Transp Porous Med (2016) 112:707–736
DOI 10.1007/s11242-016-0671-5

Semi-Analytical Modeling of Flow Behavior in Fractured Media with Fractal Geometry

Junlei Wang[1] · **Yunsheng Wei**[1] · **Yadong Qi**[1]

Received: 2 August 2015 / Accepted: 7 March 2016 / Published online: 23 March 2016

Abstract There is a gap between direct discrete fracture network numerical model and conceptual multi-linear/porosity analytical model for simulating production performance from fractured unconventional reservoirs. The principle focus of this work is on proposing a hybrid model of complexly fractured reservoir by associating fractal theory with multiple-fractured configuration. The formulation is established on the trilinear-flow idealization presented by Brown et al. (2009). Our model could account for the heterogeneity of fracture network in stimulated reservoir volume (SRV) and the arbitrary properties of multiple hydraulic fractures. Furthermore, a semi-analytical solution is correspondingly presented by incorporating Laplace–Fourier transformation and Stehfest numerical inversion based on the principle of pressure superposition. The new algorithm integrates multiple trilinear-flow solutions for single-fracture hypothesis into a general solution for multi-fractured horizontal well. The second focus is put on verification of the semi-analytical solution by comparing with alternative analytical/numerical simulations for two cases: (a) multi-fractures solution in homogeneity media; (b) multi-fractures solution in heterogeneity media with fractal characteristic. Excellent agreement between alternative simulations and our solutions is achieved. Finally, several synthetic examples are introduced to illustrate the application of semi-analytical solution in the field of pressure transient analysis and discuss the effects of the parameters on transient pressure behavior, including fracture number/spacing, conductivity, fractal characteristic constant and associated anomalous-diffusion constant. The model provides a new knowledge and insight into understanding flow behavior in fractured unconventional reservoirs.

Keywords Fractured horizontal well · Stimulated reservoir volume · Fractal geometry · Anomalous diffusion · Flow regime

✉ Junlei Wang
wangjunlei@petrochina.com.cn; williamwang_2@126.com

[1] Research Institute of Petroleum Exploration & Development, PetroChina, Beijing 100083, People's Republic of China

Nomenclature

B	Volume factor, dimensionless
d_e	Euclidean dimension, dimensionless
d_f	Fractal dimension, dimensionless
d_w	Anomalous diffusion coefficient, dimensionless
F_c	Fracture conductivity, m^3
h	Reservoir height, m
$I_v(x)$	Modified Bessel function of the first kind with order v
$K_v(x)$	Modified Bessel function of the second kind with order v
k_{SRV}	Anomalous-diffusion permeability, $m^2 \cdot s^{1-\gamma}$
k_{SRV}^{ref}	Anomalous-diffusion reference permeability, $m^2 \cdot s^{1-\gamma}$
k	Permeability, m^2
L_m	Distance measured from left-hydraulic-fracture plane, m
L_s	Fracture spacing, m
n_f	Number of hydraulic fracture
q	Production rate, m^3/s
s	Dimensionless variable in Laplace-transform domain, dimensionless
T	Temperature, K
t	Time variable, s
x	Spatial variable perpendicular to horizontal well, m
x_{HF}	Half-hydraulic-fracture length, m
x_R	Drainage area width, m
y	Spatial variable parallel to horizontal well, m
Z	Gas deviation factor, dimensionless
γ	Fractional derivative order, dimensionless
η	Diffusion capacity, m^2
θ	Scaling variable, dimensionless
μ	Viscosity, pa · s
λ	Flow capacity ratio, dimensionless
ζ	Symbol indicating right or left part within SRV unit
ρ	Density, g/m^3
φ	Porosity, dimensionless

Subscripts

D	Dimensionless
HF	Hydraulic fracture
ref	Reference parameter
SRV	Stimulated reservoir volume
XRV	External reservoir volume
w	Horizontal wellbore

Superscripts

L	Left half-hydraulic fracture in elementary SRV unit
R	Right half-hydraulic fracture in elementary SRV unit
$\sim$	Laplace transform
$\wedge$	Fourier cosine transform

1 Introduction

Unconventional reservoirs are recently becoming alternative commercial hydrocarbon production targets. The successful exploitation of these reservoirs heavily relies on the combination of horizontal drilling, multi-stage completions and innovative fracturing (Cipolla 2009; Mayerhofer et al. 2011). To maximize reservoir contact and enhance hydrocarbon production, the ultra-low permeability reservoir requires an interconnected fracture network with moderate conductivity and relatively small spacing between fractures. Because of the presence of stress isotropy and pre-existing natural fractures, stimulation treatment in unconventional reservoir generally create complex fracture network. Therefore, it is a great challenge to analyze production-decline trend and evaluate post-fracture performance in such complexly fractured reservoirs. However, direct application of traditional production performance model would unfortunately contribute to erroneous evaluation and predictions (Clarkson 2013).

To simulate hydrocarbon production from fractured reservoirs, numerical and analytical approaches were simultaneously utilized. Numerical methods include direct reservoirs numerical simulation (Cipolla et al. 2011; Weng et al. 2011) and dual continuum model with discrete fracture network (Wu et al. 2007; Monifar et al. 2013). Although numerical model provides an accurate insight into the production performance of complex fracture network (Cipolla 2009), but numerical-simulation knowledge requirement and the associated huge time-consuming computation make this method less attractive and practicable. Comparably, analytical model is a major simplification of actual physical system, which was presented in the form of multi-continuum model (Tivayanonda et al. 2012; Zhao et al. 2014) and multi-linear flow model (EI-Banbi and Wattenbarger 1998; Wattenbarger et al. 1998a; Brown et al. 2009; Bello and Wattenbarger 2010; Obinna and Hassan 2014). It is versatile enough to capture the fundamental characteristics of conducting flow throughout in fractured reservoirs. Numerous studies have confirmed that this approach has no capacity of providing accurate solutions in the presence of SRV, but is advantageous in terms of computational convenience; thus, linear flow model is recast to be applicable for analyzing production data from hydraulically fractured wells.

Compared with these standard models assuming uniform permeability throughout reservoirs, non-uniform permeability distribution was introduced to account for the complexity of the induced fracture network as the result of hydraulic fracturing operation. Under this circumstance, enhanced region model was implemented to capture the difference between stimulated and un-stimulated regions around hydraulic fractures, highlighting the nonuniform within SRV (Stalgorova and Mattar 2012, 2013). To address the concerns about the nonuniform characteristics in heterogeneous porous media, fractal theory is recently proposed to describe the fractured media, such as power-law-type variation in flow capacity [e.g., applied in RTA presented by Chang and Yortsos (1990), RTA presented by Camacho-Velázquez et al. (2008)], and linear or exponential variation in flow capacity [see Fuentes-Cruz et al. (2014a, b), 2015 for a detailed description for the single- and dual-porosity idealizations].

In this work, we establish a hybrid model combining trilinear-flow model with fractal geometry and multi-fractured configuration. This model takes into account distance-dependent properties and associated anomalous diffusion, highlighting the heterogeneity of petrophysical properties within SRV and the interaction between hydraulic fractures. Compared with previous works, the improvement of this model is threefold: (1) it relaxes the assumption of uniform permeability and porosity field for trilinear-flow model [Brown's model (2009) was built on the uniform assumption]; (2) it associates the fractal theory with

anomalous diffusion theory to account for the flow characteristics in fractured media [Cossio et al. (2013) just used fractal diffusivity equation to combine with trilinear-flow model]; (3) it fills the gap between trilinear-flow model on the symmetry hypothesis of MFHW and the actual asymmetry multi-fractured configuration [Brown's and Cossio's models were established on the symmetry hypothesis of MFHW]. The semi-analytical model could provide more reasonable and practical simulations of transient pressure response in fractured media.

2 Physical Model

2.1 Background

In the terms of fundamental research on microscopic pore structure characterization, fractal theory is implemented to characterize the randomness of pore sizes in heterogeneous porous media (Cai and Yu 2011) and determine the permeability of fibrous porous media (Cai et al. 2015). These parameters could reflect the flow paths and play an important role in flow characterization of effective diffusivity and flow resistance. To represent the uncertainty and heterogeneity in fractured porous media, fractal theory is also useful in determining the macroscopic properties of individual fractures and of fracture network (Adler and Thovert 1999). As consequence, non-local and memory effect in fractal-like structure needs to be considered to account for the associated anomalous diffusion in highly complex media with fractal geometry [seen Raghavan (2012a, b); Raghavan et al. (2013a, b); Chen and Raghavan (2013, 2015) and Ozcan et al. (2014) for the detailed explanation and analysis of fractional diffusion effect on production performance of MFHW]. Appendix 1 provides the detailed explanation on the theory of Fractal Geometry and Anomalous Diffusion.

As seen from Fig. 1, massive fracturing treatment contributes to complex fracture network; meanwhile, the density of fracture network monotonically decreases as the distance from the main fracture plane increases based on the microseismic mapping result. In addition to orthogonal fracture (wire-mesh) and discrete fracture network (DFN) techniques, for the purpose of simulating the linear-flow geometry, it is reasonable to assume that the permeability field is distance-dependent based on idealized linear model according to the valid works previously presented by Cossio et al. (2013) and Fuentes-Cruz (2014a, 2014b, 2015). Therefore, in this work, we incorporate the fractal theory and anomalous diffusion theory to characterize the feature of fluid flowing throughout fractured porous media.

2.2 Description

Figure 2 depicts the idealized MFHW model, consisting of n_f representative elementary volumes (REV). As seen in Fig. 2a, the effective drainage volume controlled by MFHW refers to the maximum areal extent contributing hydrocarbons to the well in its lifetime. In the area far beyond effective drainage area, the contribution of reservoir volume is usually negligible because of ultra-low permeability of natural fracture and matrix. Therefore, effective drainage volume is determined by eventual well spacing and fractured horizontal segment and potentially divided into three distinct regions:

(1) *Hydraulic Fractured Volume (HFV)* HFV consists of a set of discrete finite-conductivity hydraulic fractures intersected by horizontal wellbore. HFV contributes much higher conductivity and better connection with reservoirs.

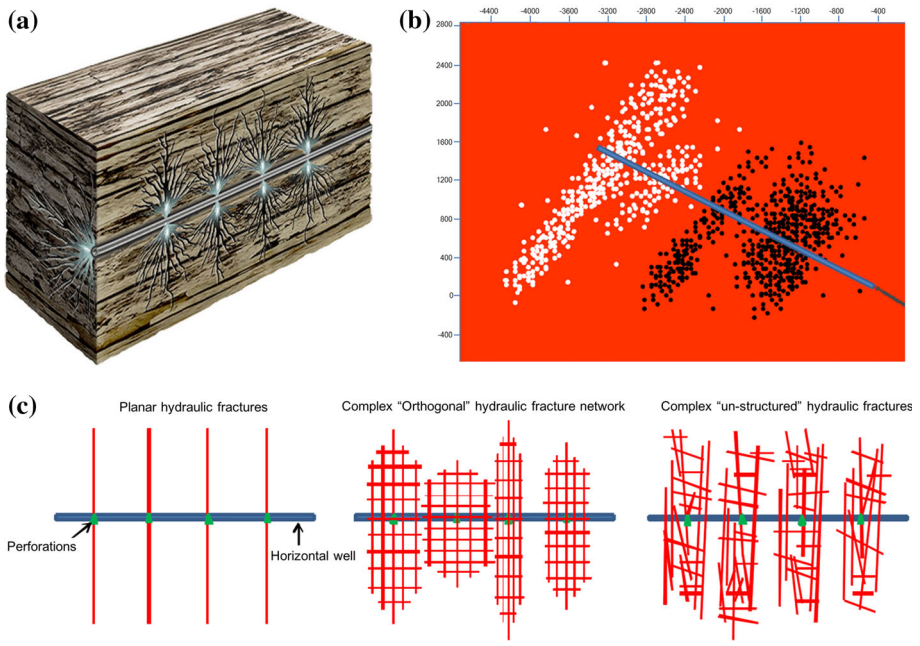

Fig. 1 Fracture network containing hydraulic and induced fracture sets. **a** Conceptual model of stimulated reservoirs volume (Fuentes-Cruz et al. 2015). **b** The distribution of induced fracture network based on micro-seismic mapping (Cipolla et al. 2012), **c** Three varying degrees of fracture network complexity (Cipolla et al. 2011)

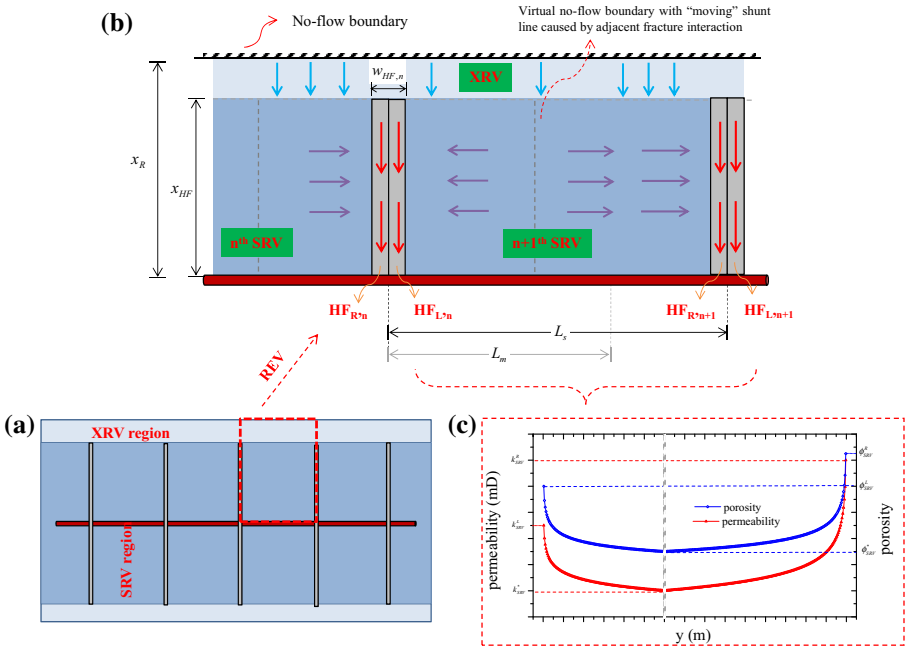

Fig. 2 Schematic of multifractured reservoirs with fractal geometry. **a** multi-fractured horizontal well in effective drainage volume (SRV & XRV & HFV). **b** *n*-th representative elementary volume (REV) within MFHW. **c** Power-law functions represent the permeability and porosity field within SRV region

(2) *Stimulated Reservoir Volume (SRV)* SRV is created in the vicinity of HFV. SRV is related to the nonuniformly distributed permeability/porosity with fractal characteristic on a wide range of scales. Generally, its areal extension is determined by perforated lateral length and dominant fracture length.
(3) *External Reservoir Volume (XRV)* XRV refers to the part of effective drainage area in addition to HFV and SRV. XRV is slightly disturbed by fracturing treatment but could contribute hydrocarbons in production lifetime. It locates in the vicinity beyond fracture tips, external to SRV region.

In Fig. 2b, on the scale of individual fracture, REV contains four parts: one SRV element, two half-width HFV elements (left-side half-width HF and right-side half-width HF), one XRV element. In Fig. 2c, the highest permeability-porosity (k^{ξ}_{SRV} and $\varphi^{\xi}_{\mathrm{SRV}}$, where $\xi = L$ indicates the value of left-side half-width HF, $\xi = R$ indicates right side) is located on the main fracture plane ($y = w_{\mathrm{HF}}/2$), and the value decreases as the distance to the fracture plane increases, until to minimum value. The minimum value (k^{*}_{SRV} and $\varphi^{*}_{\mathrm{SRV}}$) is reached at $y = L_{\mathrm{m}}$, where the energy of fracturing treatment operation dissipates to the minimum.

In this work, we represent the permeability/porosity field with regard to spatial distribution by using fractal theory, which are rewritten in a different way from Eqs. (17)–(18). They are now represented in reference of fracture plane:

$$k_{\mathrm{SRV}}(y) = k^{\mathrm{ref}}_{\mathrm{SRV}} \left(\frac{y}{L_{\mathrm{ref}}} \right)^{d_f - d_e - \theta} \tag{1}$$

$$\phi_{\mathrm{SRV}}(y) = \phi_{\mathrm{ref}} \left(\frac{y}{L_{\mathrm{ref}}} \right)^{d_f - d_e} \tag{2}$$

It is obvious that we could obtain corresponding values of d_{f} and θ through using given parameters (k^{ξ}_{SRV}, k^{*}_{SRV}, $\varphi^{\xi}_{\mathrm{SRV}}$, $\varphi^{*}_{\mathrm{SRV}}$, $L_{\mathrm{m}}, L_{\mathrm{s}}$), as follows:

$$\begin{cases} d_{f,R} = \ln\left(\frac{\phi^{*}_{\mathrm{SRV}}}{\phi^{\mathrm{R}}_{\mathrm{SRV}}} \right) \ln^{-1}\left(\frac{L_s - L_m}{w_{\mathrm{HF}}/2} \right) + d_e \\ d_{f,\mathrm{L}} = \ln\left(\frac{\phi^{*}_{\mathrm{SRV}}}{\phi^{\mathrm{L}}_{\mathrm{SRV}}} \right) \ln^{-1}\left(\frac{L_m}{w_{\mathrm{HF}}/2} \right) + d_e \end{cases} \tag{3}$$

$$\begin{cases} \theta_R = \ln^{-1}\left(\frac{L_s - L_m}{w_{\mathrm{HF}}/2} \right) \ln\left(\frac{\phi^{*}_{\mathrm{SRV}} k^{\mathrm{R}}_{\mathrm{SRV}}}{\phi^{\mathrm{R}}_{\mathrm{SRV}} k^{*}_{\mathrm{SRV}}} \right) \\ \theta_{\mathrm{L}} = \ln^{-1}\left(\frac{L_m}{w_{HF}/2} \right) \ln\left(\frac{\phi^{*}_{\mathrm{SRV}} k^{\mathrm{L}}_{\mathrm{SRV}}}{\phi^{\mathrm{L}}_{\mathrm{SRV}} k^{*}_{\mathrm{SRV}}} \right) \end{cases} \tag{4}$$

It is noted that we recast three regions with different characterized geometries [e.g., finite-conductivity HFV, fractal-like media for SRV, and uniform media for XRV] for the purpose of highlighting each other's distinction as a consequence of the fracturing treatment operation.

3 Mathematical Model

The new formulation of MFHW is established based on multiple trilinear-flow models with fractal geometry. Each individual trilinear-flow model corresponds to a REV as seen in Fig. 2b. For single REV, we derive the solutions for the XRV, SRV and HFV sequentially, and then couple the solutions by using the flux- and pressure-continuity conditions on the interface between the regions. And then, we couple the solutions for multiple REVs by using pressure

superposition principle on the basis of flux restriction and infinite-conductivity wellbore assumption.

According to the descriptions above, some idealizations and simplifying assumptions are summarized as follows:

- An isotropic, horizontal, slap gas reservoir is bounded by overlying and underlying impermeable strata;
- The height of HFV, SRV and XRV is assumed to be same as the strata height;
- The petrophysical properties in XRV are homogeneous and identical (i.e., permeability and porosity is uniform);
- HFV connects to horizontal wellbore, and HF wings are symmetrically spaced with regard to horizontal wellbore. Correspondingly, production from the surface of horizontal wellbore might be negligible;
- The production process is isothermal, and matrix and fracture network are considered incompressible compared to gas compression.

3.1 Solution for Single REV

3.1.1 External Reservoir Volume with Continuum

Within XRV, the volume is less slightly fractured compared with SRV due to the decrement of fracturing treatment. Hence, fracture network within XRV is modeled as continuum media, where fractures interconnect with each other.

After incorporating dimensionless definitions in Appendix 1, the dimensionless pressure governing equation in Laplace-transform domain is satisfied as follows:

$$\frac{\partial^2 \tilde{p}_{\mathrm{XRVD}}}{\partial x_{\mathrm{D}}^2} = \frac{s}{\eta_{\mathrm{XRVD}}} \tilde{p}_{\mathrm{XRVD}} \tag{5}$$

Appendix 3 provides the details of derivation for Eq. (5). Thus we could obtain the dimensionless flux on interface between SRV and XRV, which is given as

$$\left(\frac{\partial \tilde{p}_{\mathrm{XRVD}}}{\partial x_{\mathrm{D}}} \right) \Bigg|_{x_{\mathrm{D}}=x_{\mathrm{HFD}}} = -\tilde{F}_{\mathrm{SRV}}^{\mathrm{XRV}} \left(\tilde{p}_{\mathrm{SRVD}} \right) |_{x_{\mathrm{D}}=x_{\mathrm{HFD}}} \tag{6}$$

where $\tilde{p}_{\mathrm{XRVD}}$ represents the dimensionless pressure of XRV, $\tilde{p}_{\mathrm{SRVD}}$ represents the dimensionless pressure of XRV, s represents the Laplace variable, η_{XRVD} represents the diffusion capacity of XRV, x_{HFD} represents the dimensionless half-length of hydraulic fracture, and $\tilde{F}_{\mathrm{SRV}}^{\mathrm{XRV}}$ is the characteristic function, which represents the dimensionless flux from XRV to SRV.

3.1.2 Stimulated Reservoir Volume with Fractal Fracture Network

A representative unit of SRV is selected as the element of MFHW, defined as REV. Within one REV, related variables to fracture are distinguished by superscript denoted as R and L. After incorporating Laplace transformation, the flow equation in SRV is given in the following form of dimensionless pressure, this is

$$\frac{\partial^2 \tilde{p}_{\mathrm{SRVD}}^{\xi}}{\partial y_{\mathrm{D}}^2} + \frac{d_{f,\xi} - d_e - \theta_\xi}{y_{\mathrm{D}}} \frac{\partial \tilde{p}_{\mathrm{SRVD}}^{\xi}}{\partial y_{\mathrm{D}}} = y_{\mathrm{D}}^{\theta_\xi} \left(\frac{s^{\gamma_\xi}}{\eta_{\mathrm{SRVD}}^{\xi}} + \frac{\lambda_{\mathrm{SRV},\xi}^{\mathrm{XRV}} \tilde{F}_{\mathrm{SRV},\xi}^{\mathrm{XRV}}}{s^{1-\gamma_\xi}} \right) \tilde{p}_{\mathrm{SRVD}}^{\xi} \tag{7}$$

where, ξ indicates R or L, where R represents the right-side SRV region in REV, L represents left-side. $d_{f,\xi}$ indicates fractal dimension in the left- or right-side SRV region, θ_ξ indicates scaling variable in the left- or right-side SRV region, $\gamma_{f,\xi}$ indicates fractional derivative order in the left- or right-side SRV region, d_e indicates Euclidean dimension. $\tilde{p}^{\xi}_{\mathrm{SRVD}}$ represents dimensionless pressure in the left- or right-side SRV region, $\tilde{p}^{\xi}_{\mathrm{HFD}}$ represents dimensionless pressure in the left- or right-side HF. $\eta^{\xi}_{\mathrm{SRVD}}$ represents the diffusion capacity of the left- or right-side SRV region, $\lambda^{\mathrm{XRV}}_{\mathrm{SRV},\xi}$ indicates flow capacity ratio of XRV to the left- or right-side SRV region. $\tilde{F}^{\mathrm{XRV}}_{\mathrm{SRV},\xi}$ is the characteristic function, which represents the dimensionless flux from XRV to the left- or right-side SRV region, $\tilde{F}^{\mathrm{SRV}}_{\mathrm{HF},\xi}$ is the characteristic function, which represents the dimensionless flux from the left- or right-side SRV region to corresponding HF.

Appendix 4 presents the detailed derivation of solutions for Eq. (7). Therefore, the dimensionless influx from SRV into HF could be obtained. As seen in Fig. 2a, MHFW consists of two kinds of REV: inner REV and outermost REV (i.e., including one half-width fracture). For outermost REV in MFHW,

$$\left(\frac{\partial \tilde{p}^{\xi}_{\mathrm{SRVD}}}{\partial y_{\mathrm{D}}}\right)\Bigg|_{y_{\mathrm{D}}=0.5w_{\mathrm{HFD}}} = -\tilde{F}^{\mathrm{SRV}}_{\mathrm{HF},\xi}\left(\tilde{p}^{\xi}_{\mathrm{HFD}}\Big|_{y_{\mathrm{D}}=0.5w_{\mathrm{HFD}}}\right) \tag{8a}$$

For inner REV,

$$\left(\frac{\partial \tilde{p}^{\mathrm{L}}_{\mathrm{SRVD}}}{\partial y_{\mathrm{D}}}\right)\Bigg|_{y_{\mathrm{D}}=0.5w_{\mathrm{HFD}}} = \tilde{F}^{\mathrm{SRV}}_{\mathrm{HF},\mathrm{R}1}\left(\tilde{p}^{\mathrm{R}}_{\mathrm{HFD}}\Big|_{y_{\mathrm{D}}=0.5w_{\mathrm{HFD}}}\right) - \tilde{F}^{\mathrm{SRV}}_{\mathrm{HF},L1}\left(\tilde{p}^{\mathrm{L}}_{\mathrm{HFD}}\Big|_{y_{\mathrm{D}}=0.5w_{\mathrm{HFD}}}\right) \tag{8b}$$

$$\left(\frac{\partial \tilde{p}^{\mathrm{R}}_{\mathrm{SRVD}}}{\partial y_{\mathrm{D}}}\right)\Bigg|_{y_{\mathrm{D}}=0.5w_{\mathrm{HFD}}} = \tilde{F}^{\mathrm{SRV}}_{\mathrm{HF},R2}\left(\tilde{p}^{\mathrm{R}}_{\mathrm{HFD}}\Big|_{y_{\mathrm{D}}=0.5w_{\mathrm{HFD}}}\right) - \tilde{F}^{\mathrm{SRV}}_{\mathrm{HF},L2}\left(\tilde{p}^{\mathrm{L}}_{\mathrm{HFD}}\Big|_{y_{\mathrm{D}}=0.5w_{\mathrm{HFD}}}\right) \tag{8c}$$

The effect of fracture–production interaction is further decomposed into two parts: (a) interaction between adjacent fractures within REV, (b) interaction between adjacent REVs. Section 3.1.2 only accounts for the effect of interaction between adjacent fractures within REV. The adjacent REV interaction would be presented in Sect. 3.2, which is considered by incorporating pressure superposition principle.

3.1.3 Hydraulic Fractured Volume with Discrete Fractures

Utilizing modified Darcy law in Laplace domain, Eq. (20), the dimensionless pressure governing equation of fracture is given in the following dimensionless form.

$$\frac{\partial^2 \tilde{p}^{\xi}_{\mathrm{HFD}}}{\partial x^2_{\mathrm{D}}} + 2\frac{\lambda^{\mathrm{SRV}}_{\mathrm{HF},\xi}}{s^{\gamma_\xi - 1}}\left(\frac{\partial \tilde{p}^{\xi}_{\mathrm{SRVD}}}{\partial y_{\mathrm{D}}}\right)\Bigg|_{y_{\mathrm{D}}=0.5w_{\mathrm{HFD}}} = \frac{s}{\eta^{\xi}_{\mathrm{HFD}}}\tilde{p}^{\xi}_{\mathrm{HFD}} \tag{9}$$

where, ξ indicates R or L, where R represents the right-side SRV region in REV, L represents left-side. $\tilde{p}^{\xi}_{\mathrm{HFD}}$ represents the dimensionless pressure of the right- or left- side hydraulic fracture, η^{ξ}_{HFD} represents the diffusion capacity of the left- or right-side hydraulic fracture, $\lambda^{\mathrm{SRV}}_{\mathrm{HF},\xi}$ indicates flow capacity ratio of the left- or right-side SRV to corresponding HF.

Appendix 4 provides the detailed derivation of Eq. (9). The dimensionless pressure distribution along hydraulic fracture is subsequently given. For outermost REV,

$$\tilde{p}^{\xi}_{\mathrm{HFD}}(x_{\mathrm{D}}) = \frac{2\pi \tilde{q}^{\xi}_{\mathrm{HFD}}}{C^{\xi}_{\mathrm{HFD}}} \frac{\coth\left(x_{\mathrm{HFD}}\sqrt{s/\eta^{\xi}_{\mathrm{HFD}} + 2\lambda^{\mathrm{SRV}}_{\mathrm{HF},\xi}\tilde{F}^{SRV}_{HF,\xi}/s^{\gamma_\xi - 1}}\right)}{\sqrt{s/\eta^{\xi}_{\mathrm{HFD}} + 2\lambda^{\mathrm{SRV}}_{\mathrm{HF},\xi}\tilde{F}^{\mathrm{SRV}}_{\mathrm{HF},\xi}/s^{\gamma_\xi - 1}}} \tag{10a}$$

For inner REV,

$$\tilde{p}^{\mathrm{L}}_{\mathrm{HFD}}(x_{\mathrm{D}}) = \tilde{q}^{\mathrm{L}}_{\mathrm{HFD}} A X^{\mathrm{L}}_{\mathrm{SRV}}(x_{\mathrm{D}}) + \tilde{q}^{\mathrm{R}}_{\mathrm{HFD}} B X^{\mathrm{L}}_{\mathrm{SRV}}(x_{\mathrm{D}}) \tag{10b}$$

$$\tilde{p}^{\mathrm{R}}_{\mathrm{HFD}}(x_{\mathrm{D}}) = \tilde{q}^{\mathrm{L}}_{\mathrm{HFD}} B X^{\mathrm{R}}_{\mathrm{SRV}}(x_{\mathrm{D}}) + \tilde{q}^{\mathrm{R}}_{\mathrm{HFD}} A X^{\mathrm{R}}_{\mathrm{SRV}}(x_{\mathrm{D}}) \tag{10c}$$

It is noted that the solutions above are presented based on vertical fracture. This is different from transverse fracture intersecting horizontal wellbore, which results in the additional pressure drop around horizontal wellbore. The effect could be taken into account by modifying Eqs. (10a)–(10c) according to the method presented by Wang et al. (2016).

3.2 Solution for Multiple REVs

The multiple-fractures system is divided into several independent REV. According to the superposition principle, pressure distribution caused by n_{f} fractures can be written in Laplace domain as follows,

$$\tilde{p}_{Dj,i} = \sum_{i=1}^{n_f} \tilde{q}^{\mathrm{L}}_{\mathrm{HFD},i} \Delta \tilde{p}^{\mathrm{L}}_{Dj,i} + \sum_{i=1}^{n_f} \tilde{q}^{\mathrm{R}}_{\mathrm{HFD},i} \Delta \tilde{p}^{\mathrm{R}}_{Dj,i} \tag{11}$$

where subscript "j, i" indicates dimensionless pressure response of the j-th fracture caused by the production of the i-th fracture. Based on the assumption of infinite-conductivity wellbore, the dimensionless pressure on the interface between each hydraulic fracture and wellbore is equal to wellbore pressure p_{wD}.

$$\tilde{p}_{wD,1} = \tilde{p}_{wD,2} = \cdots = \tilde{p}_{wD,n_f} = \tilde{p}_{wD} \tag{12}$$

In the condition of constant flow rate for multiple-fractures system, the additional condition yields the following expression in Laplace domain

$$\sum_{i=1}^{n_f} \tilde{q}^{\mathrm{L}}_{\mathrm{HFD},i} + \sum_{i=1}^{n_f} \tilde{q}^{\mathrm{R}}_{\mathrm{HFD},i} = \frac{1}{s} \tag{13}$$

Thus, we can obtain the following matrix by combining Eq. (11)–(13), which is

$$\mathbf{A}\vec{\mathbf{X}} = \vec{\mathbf{d}} \tag{14}$$

where

$$\mathbf{A} = \begin{bmatrix} \mathbf{A}_1 & & & -\mathbf{B}_1 \\ & \mathbf{A}_2 & & -\mathbf{B}_2 \\ & & \ddots & \vdots \\ & & & \mathbf{A}_{n_f+1} \ -\mathbf{B}_{n_f+1} \\ \mathbf{B}_1^{\mathbf{T}} & \mathbf{B}_2^{\mathbf{T}} & \cdots & \mathbf{B}_{n_f+1}^{\mathbf{T}} \quad 0 \end{bmatrix}, \quad \vec{\mathbf{X}} = \begin{bmatrix} \mathbf{X}_1 \\ \mathbf{X}_2 \\ \vdots \\ \mathbf{X}_{n_f+1} \\ s\tilde{p}_{wD} \end{bmatrix}, \quad \vec{\mathbf{d}} = \begin{bmatrix} \mathbf{0} \\ \mathbf{0} \\ \vdots \\ \mathbf{0} \\ 1 \end{bmatrix} \tag{15a}$$

where bold types in Eq. (14) indicate vectors and matrixes. The i-th element in matrix $\mathbf{A}$ represents the i-th REV, which can be further expressed as,

$$\mathbf{A}_i = \begin{cases} AX_{\mathrm{SRV}}^{\mathrm{R},1}, & i = 1 \\ \begin{bmatrix} AX_{\mathrm{SRV}}^{\mathrm{L},i} & BX_{\mathrm{SRV}}^{\mathrm{L},i} \\ BX_{\mathrm{SRV}}^{\mathrm{R},i} & AX_{\mathrm{SRV}}^{\mathrm{R},i} \end{bmatrix}, & 2 \le i \le n_f \\ AX_{\mathrm{SRV}}^{\mathrm{L},n_f+1}, & i = n_f + 1 \end{cases} \tag{15b}$$

and element $\mathbf{B}$ represents the constraint of Eq. (13), which is given as

$$\mathbf{B}_i = \begin{cases} 1, & i = 1 \text{ and } n_f + 1 \\ \begin{bmatrix} 1 & 1 \end{bmatrix}^{\mathrm{T}}, & 2 \le i \le n_f \end{cases} \tag{15c}$$

In addition, dimensionless rate vector $\mathbf{X}$ of single half-width fracture is expressed as

$$\mathbf{X}_i = \begin{cases} s\tilde{q}_{\mathrm{HFD}}^{\mathrm{R},1}, & i = 1 \\ \begin{bmatrix} s\tilde{q}_{\mathrm{HFD}}^{\mathrm{L},i-1} & s\tilde{q}_{\mathrm{HFD}}^{\mathrm{R},i} \end{bmatrix}^{\mathrm{T}}, & 2 \le i \le n_f \\ s\tilde{q}_{\mathrm{HFD}}^{\mathrm{L},n_f}, & i = n_f + 1 \end{cases} \tag{15d}$$

By solving Eq. (14), we can obtain the unknown wellbore pressure and the flow rate distribution of hydraulic fractures in real-time domain by integrating Newton iteration method and Stehfest numerical inversion algorithm (Stehfest 1970).

4 Model Validation

In this section, two alternative simulations are selected to validate our model. It needs to be emphasized that multi-linear model has no capacity of simulating pseudo-radial flow regime in infinite-acting reservoirs, so it must be generated in a finite reservoir with no-flow boundaries. The constraint condition is generally set to be $0.7 \le (x_{\mathrm{HF}}/x_{\mathrm{R}}) \le 1$. It indicates boundary-dominant flow would emerge in advance before pseudo-radial flow regime occurs. Song et al. (2011) had affirmed that constraint condition is reasonable and reliable in the practice of fracturing treatment operation. In this section, C_{fD} is redefined as $(k_{\mathrm{HF}} w_{\mathrm{HF}})/(k_{\mathrm{XRV}} x_{\mathrm{HF}})$.

4.1 Analytical Validation

In our work, the homogeneity case refers to Euclidean dimension and classical diffusion in the symmetry configuration of equally spaced fractures with identical properties (fracture width, length, conductivity, etc.), which is given as

$$d_e = 1,\ d_f = 1,\ \gamma = 1,\ \theta = 0;\ L_{mD} = 0.5 L_{sD} \tag{16}$$

When the parameters of REV left region are identical to the right under homogeneity case, the multi-fractures solution completely converges to conventional MFHW solution. Because we have not found identical published papers to our model, the validation of homogeneity case is conducted firstly, which is conducted by comparing with the result of Brown et al. (2009). Noted that the transformations of parameters between two models, they are list as: $\eta_{\mathrm{XRVD}} = \eta_{\mathrm{oD}}$, $\eta_{\mathrm{SRVD}} = 1$, $\eta_{\mathrm{HFD}} = \eta_{\mathrm{FD}}$, $\lambda_{\mathrm{SRV}}^{\mathrm{XRV}} = \frac{1}{y_{\mathrm{eD}} C_{\mathrm{RD}}}$, $\lambda_{\mathrm{HF}}^{\mathrm{SRV}} = \frac{1}{C_{\mathrm{FD}}}$, $L_{\mathrm{sD}} = y_{\mathrm{eD}}$, $x_{\mathrm{RD}} = x_{eD}$, $x_{\mathrm{HFD}} = 1$ (the parameters in the right hand side are quoted from Brown's model). As seen in Fig. 3, the model shows excellent agreement with Brown's results in

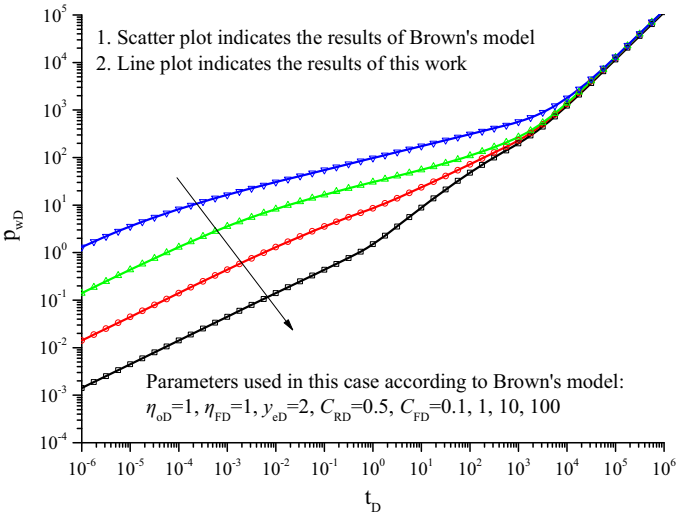

Fig. 3 Comparison of analytical solution for single fracture with Brown's solution in homogeneity case

Table 1 Basic parameters used for model validation

Basic model parameter	Value	Basic model parameter	Value
Formation width, x_R(m)	127.55	Fracture porosity, φ_f(%)	35
Formation thickness, h(m)	2.9	Production rate, q_{sc}(m^3/s)	1.157×10^{-5}
Formation permeability, k_m(m^2)	10^{-17}	Initial pressure, p_i(Pa)	1×10^8
Formation porosity, φ(%)	10	Viscosity of fluid, μ(Pa · s)	0.001
Fracture width, w_{HF}(m)	0.0127	Total compressibility, c_t(Pa^{-1})	4.35×10^{-10}
Fracture half-length, x_{HF}(m)	114.95		

terms of dimensionless pressure and pressure derivatives throughout the whole time domain under different fracture conductivities.

4.2 Numerical Validation

To verify the model with fractal-like permeability/porosity field, the black oil simulator and local grid refinement have been induced. In the simulator, we simulate the transient pressure response of MFHW with 5 fractures, and fracture system is made up 5 fractures with different conductivity in the unequally spaced configuration. The basic model parameters are list in Table 1.

Here, numerical validation aims to verify the solutions under two cases: uniform permeability/porosity case and fractal-like permeability permeability/porosity case. In the uniform permeability/porosity case, there are three conditions, including (a) 5 fractures with identical conductivity in unequally spaced configuration, (b) 5 fractures with different conductivities in equally spaced configuration, (c) 5 fractures with different conductivities in unequally spaced configuration. Figure 4 shows the comparison results under three conditions in the uniform permeability/porosity case.

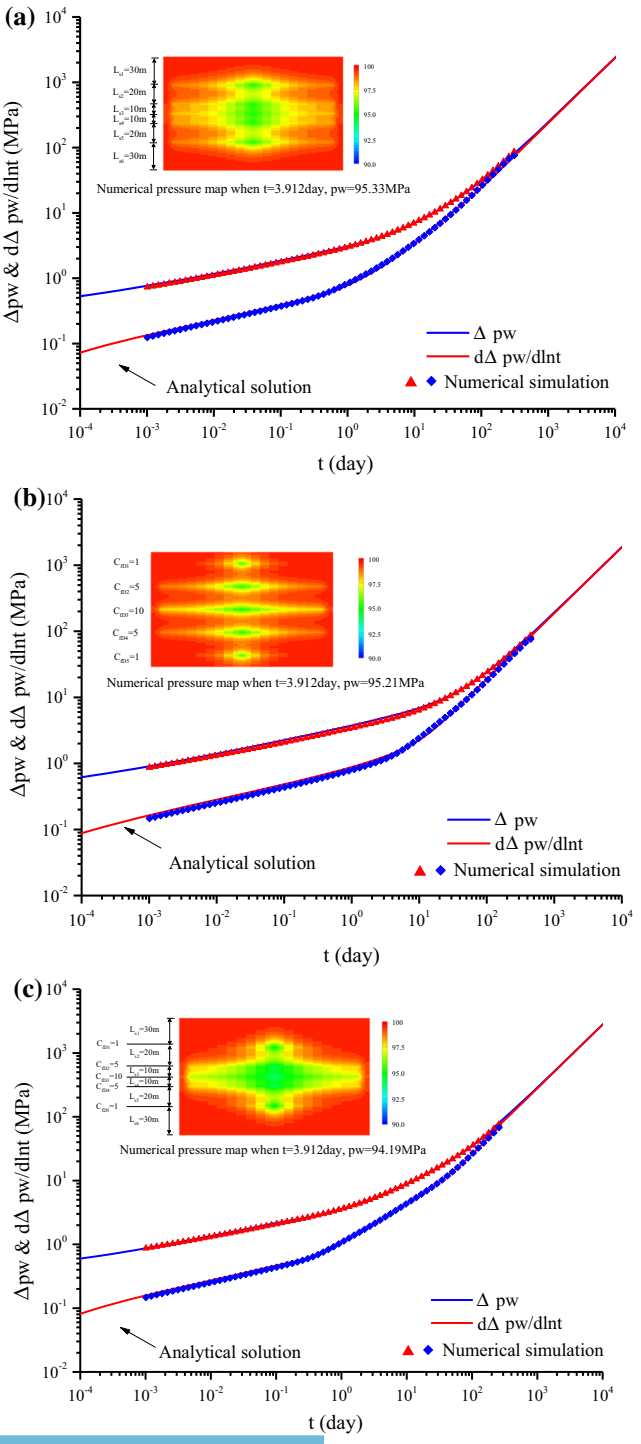

Fig. 4 Comparison of analytical solution for MFHW with numerical solution under uniform permeability/porosity case

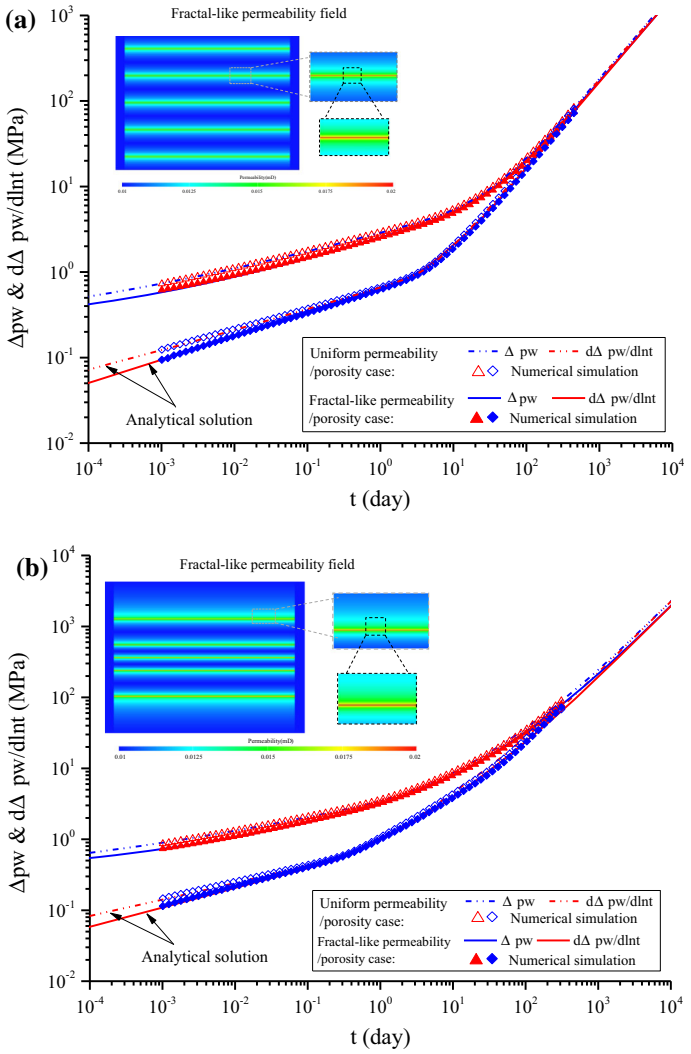

Fig. 5 Comparison of analytical solution for MFHW with numerical solution under fractal-like permeability/porosity case

In the fractal-like permeability permeability/porosity case, there are two conditions, including (a) 5 fractures with identical conductivity in equally spaced configuration, (b) 5 fractures with different conductivity in unequally spaced configuration. On fracture face, the permeability is set to be 0.02 mD and porosity to be 20 %. On the intersection between left- and right-side regions in SRV, the permeability equals to the value of XRV, 0.01mD; porosity also equals to the value of XRV, 10 %. Using Eqs.(8)–(9), we can obtain permeability/porosity field within SRV, and corresponding fractal parameters ($d_e = 1$, $d_{f,L} = d_{f,R} = 0.8816$, $\theta_L = \theta_R = 0$, $\gamma_L = \gamma_R = 1$). Figure 5 shows the comparison results under two conditions in fractal-like permeability/porosity field. As shown in Figs. 4 and 5, there are good agreements between analytical solutions and the numerical solutions under different cases. It is verified that the semi-analytical model with fractal geometry is reasonable and reliable.

Table 2 Basic dimensionless data used for Fig. 6, 7, 8 and 9

Basic dimension parameter	Symbol	Value
Formation width	x_{RD}	1000
Fracture number	n_f	5
Fracture spacing	L_s	2
Fracture half-length	x_{HFD}	1
Fracture width	w_{HFD}	0.001
Fracture conductivity	C_{HFD}	$10^{-2}, 10^{-1}, \ldots, 10^{4}$
Hydraulic fracture diffusivity	η_{HFD}	$10^{1}, 10^{0}, \ldots, 10^{6}$
SRV diffusivity	η_{SRVD}	1
XRV diffusivity	η_{XRD}	0.05
Flow capacity ratio of SRV–HF	λ_{HF}^{SRV}	$10^{-4}, 10^{-3}, \ldots, 10^{2}$
Flow capacity ratio of XRV–SRV	λ_{SRV}^{XRV}	0.5
Production rate of MFHW	q_{wD}	1
Euclidean dimension	d_e	1
Fractal dimension	d_f	$0.5, 0.6, \ldots, 1$
Scaling variable	θ	0
Fractional derivative order	γ	$0.5, 0.6, \ldots, 1$

5 Results and Discussions

The advantage of our model is to account for heterogeneity and arbitrary of fracture system, including the non-uniform distribution of permeability/porosity field in SRV, and the different properties of fracture (width, permeability, HF number/spacing, etc.). We would present some synthetic examples to illustrate the application of new model by analyzing transient pressure response. In this section, we mainly discuss the effect of fractal characteristic and anomalous diffusion on transient pressure response under two conditions in terms of hydraulic fracture: fracture conductivity and fracture number/spacing. For simplicity, we assume that fractures have identical properties in the equally spaced configuration, and the properties of SRV permeability/porosity are symmetrically distributed within one REV. It is noted that the basic parameters are list in Table 2. To make the flow regimes clearer, the formation width is set to be very large ($x_R = 1000$) to avoid the appearance of boundary-dominant flow within observed flow duration.

5.1 Effect of Hydraulic-Fracture Conductivity

As mentioned previously, the effect of fracture conductivity in uniform permeability/porosity case has been recognized in previous literature (Chen and Raghavan 1997; Zhao et al. 2014). In this illustration, seven values of dimensionless fracture conductivity are considered, where five fractures are equally spaced and dimensionless distance between outermost fractures is set to be 100.

Firstly, it is necessary to discuss the impact of fracture conductivity on transient pressure behavior in uniform case (Euclidian geometry and classical diffusion). It is the basis of further discussion. Here, we identify the flow regime evolution in uniform case by analyzing the pressure derivatives, as shown in Fig. 6a for dash lines. It is found that all curves can

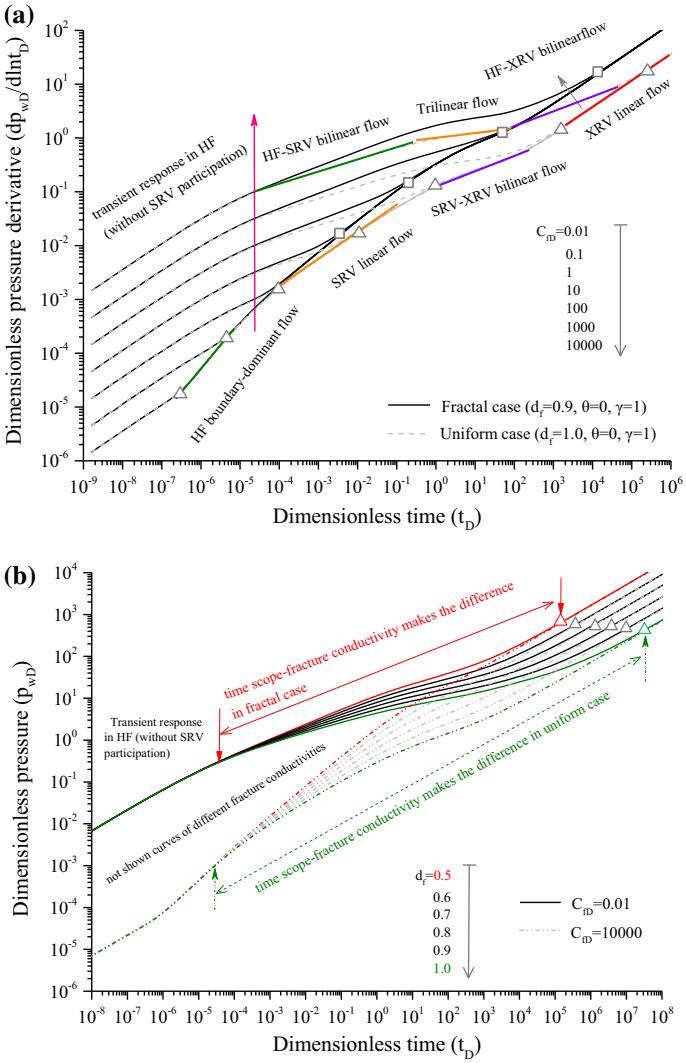

Fig. 6 **a** Effect of HF conductivity on flow regime evolution under fractal and uniform cases. **b** Effect of fractal dimension on pressure in large/small fracture conductivity condition

be divided into three parts: early-time flow regime, intermediate-time flow regime and late-time flow regime. At early-time period, the transient response in fracture is dominant without SRV participation, while the transient response in XRV would be dominant at late-time period after the responses in HF and SRV both reach the boundary-dominant state. Noted that late-time flow regimes are not affected by fracture conductivity, and fracture conductivity mainly affects the type, sequence and duration of early and intermediate-time flow regimes.

For smaller fracture conductivity (e.g. $C_{fD} = 0.01$ in uniform case), HF-SRV bilinear flow ($t_D \approx 4 \times 10^{-5}$–0.2), HF-SRV-XRV trilinear flow ($t_D \approx 0.5$–30), and HF-XRV bilinear linear ($t_D \approx 10^2$–4×10^4) could be subsequently observed at intermediate time period. Here, HF-SRV bilinear flow is caused by transient response in both HF and SRV without XRV

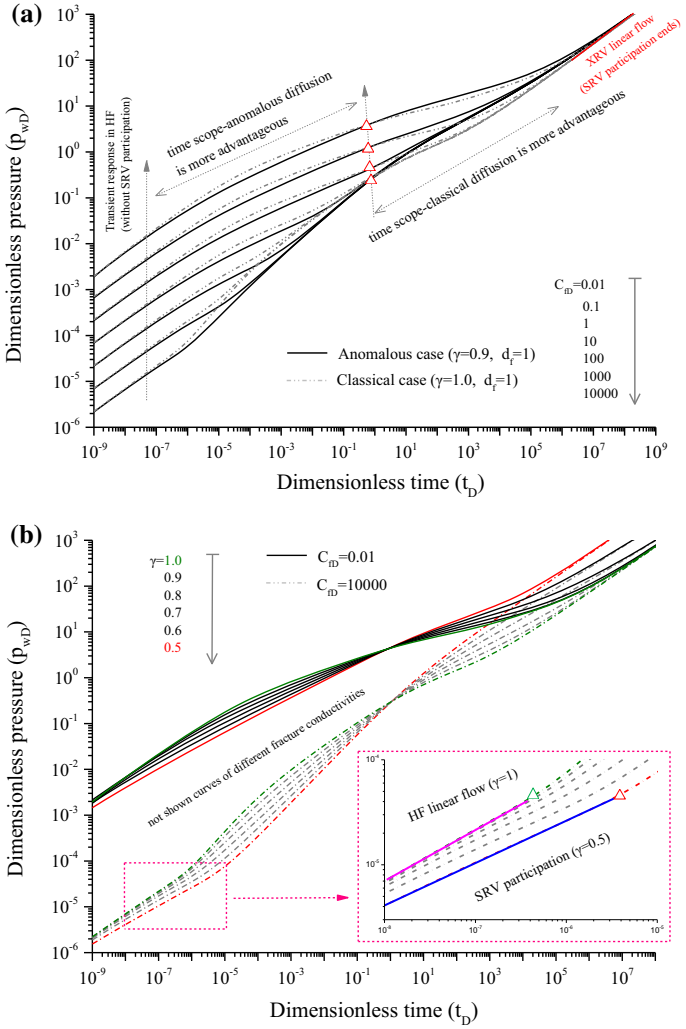

Fig. 7 **a** Effect of fracture conductivity on pressure in anomalous and classical cases. **b** Effect of anomalous diffusion index on pressure in large/small fracture conductivity cases

participation; HF-SRV-XRV trilinear flow is caused by transient response in HF, SRV and XRV; HF-XRV bilinear flow is caused by transient response in HF and XRV after SRV reaches boundary-dominant state. With fracture conductivity increasing, duration of trilinear flow gradually shortens until disappear, which contributes to a transition ($t_D \approx 1$–10) from HF-SRV bilinear flow to HF-XRV bilinear flow in the absence of trilinear flow when $C_{fD} = 1$. As HF conductivity further increases, there would appear SRV linear flow (fracture reaches boundary-dominant flow and XRV participation is too be weak to be neglected) and HF boundary-dominant flow (without SRV and XRV participation), while the duration of HF-XRV bilinear flow could further shorten and would disappear for $C_{fD} \geq 10$.

In summary, fracture conductivity increasing would contribute to the occurring of fracture boundary-dominant flow in advance, denoted by gray triangle/square as seen in Fig. 6a;

Taking example for uniform case, starting time of fracture boundary-dominant flow changes from $t_D \approx 3 \times 10^5$ for $C_{fD} = 10^4$ to $t_D \approx 2 \times 10^3$ for $C_{fD} = 10^3$, and the smallest starting time is $t_D \approx 3 \times 10^{-7}$ for $C_{fD} = 0.01$.

5.1.1 Fractal Case

Figure 6a shows the effect of fracture conductivity on pressure derivative in the condition of fractal case ($d_f < 1$), denoted by unbroken lines. During early-time period, the transient response in SRV is not taken into account, so the pressure derivatives for fractal case overlap with uniform case as mentioned above. As soon as the fluid in SRV participates in the flowing process, the derivatives would deviate from uniform case. During the deviation period, the fractal case contributes to greater pressure depletion, which is identified by the characterized straight with larger slope compared with uniform case. During the late-time period, pressure derivative for different conditions of HF conductivity overlaps again with each other. In addition, the starting time of HF boundary-dominant flow for fractal case (denoted by gray squares) accelerates to occur, and the time gap between uniform case and fractal case would be more obvious as HF conductivity decreases.

In order to further discuss the effect of fractal characteristic, Fig. 6b provides an illustration including six values of fractal dimension index d_f. It needs to be emphasized that unbroken lines indicate the pressure curves of different fractal dimensions when $C_{fD} = 0.01$, and dash lines indicate the pressure curves of different fractal dimensions when $C_{fD} = 10000$. The overlapping of curves between $C_{fD} = 0.01$ and 10000 represents the late-time SRV linear flow; thus, for same fractal dimension, the vacancy between $C_{fD} = 0.01$ and 10000 represents not shown curves of different fracture conductivities, be similar to Fig. 6a. We find that the smaller fractal dimension index is, the greater pressure depletion is, which is identified by a bigger-slope straight. Besides, the gray triangles represent the starting time of late-time SRV linear flow for smaller fracture conductivity. It indicates that changing fracture conductivity makes evident difference on the pressure depletion within early-time scope in the case of stronger fractal structure (smaller value of d_f). Put another way, the fracture conductivity plays a more important role at early-time period in fractal permeability/porosity reservoirs.

5.1.2 Anomalous Diffusion Case

Figure 7a shows the effect of fracture conductivity on pressure for the anomalous diffusion case of $\gamma < 1$ incorporating the influence of memory. Compared with Sect. 5.1.1, we find that there are intersects between anomalous diffusion ($\gamma < 1$) and classical diffusion ($\gamma = 1$), which is consistent with the conclusion of Raghavan and Chen (2013a) that "the characteristic of intersect is typical of solutions that are governed by fractional diffusion". At early-time period when HF linear flow period finishes, the pressure depletion of anomalous diffusion is smaller than classical diffusion, but would subsequently become greater at the time scope where starting time is the intersect time. Therefore, anomalous diffusion is advantage in the terms of reducing pressure depletion in smaller.

Figure 7b further displays the influence of anomalous diffusion. The overlapping of curves between $C_{fD} = 0.01$ and 10000 represents the late-time SRV linear flow; thus, for same anomalous diffusion index, the vacancy between $C_{fD} = 0.01$ and 10000 represents not shown curves of different fracture conductivities, be similar to Fig. 7a. The most important results for anomalous diffusion are twofold: (a) the smaller the anomalous diffusion index γ is, the early the pressure response deviates from classical diffusion case. For example, the ending time

of HF linear flow in the condition of larger HF conductivity is at $t_D \approx 4 \times 10^{-7}$ for $\gamma = 1$, but SRV has fully participated in the flowing process at the same time for $\gamma = 0.5$; (b) the duration of intermediate-time period decreases as anomalous diffusion index γ decreases. For instance, intermediate-time flow regimes ($C_{fD} = 10^4$, $\gamma = 0.5$), consisting of HF boundary-dominant flow, SRV linear flow and SRV-XRV bilinear flow, are not identified obviously. Thus it appears possible to explain the feature of long linear trends in unconventional gas reservoirs; for example, the duration of linear flow lasts from $t_D \approx 2 \times 10^{-5}$ to $t_D \approx 10$ for $\gamma = 0.5$ in the condition of larger HF conductivity.

5.2 Effect of Hydraulic-Fracture Number

Figure 8 shows the effect of fracture number/fracture spacing in the configuration of MFHW. In this illustration, the variable of interest is the fracture number ($n_f = 2, 3, 4, 5$), and the dimensionless distance between outermost fractures is set to be fixed 100. In the figures, dashed lines represent the pressure behavior of uniform case, and unbroken line indicates corresponding transient pressure (derivative) response in fractal and anomalous cases. In essence, fracture number has influence on pressure behavior mainly by creating the connected fracture area to reservoir and generating fracture interaction. Generally, the whole flow regime can be divided into two parts according to fracture interaction: with fracture–production interaction and without fracture–production interaction. Before fracture–production interaction, the pressure behavior is determined by the individual fracture, where the value of pressure is proportional to fracture number. As soon as fracture–production interacts, some flow regime might disappear or appear, and the duration of flow regime would also shorten or elongate, dependent on fracture number.

5.2.1 Fractal Case

Figure 8 shows the impact of fracture number on transient pressure behavior under fractal case. From the perspective of pressure depletion, if strong-interconnected SRV (perfectly, homogeneity case) was created, the effect of HF number would be less obvious. Correspondingly, the curves for homogeneity case are distributed more closely than fractal case in semi-log coordinate of Fig. 8a. In the contrary, if weak-interconnected SRV is created, increasing HF number/decreasing fracture spacing would reduce the pressure depletion dramatically. Compared with Fig. 8a, Fig. 8b shows that all curves for large fracture conductivity are distributed more closely than small fracture conductivity. It indicates that increasing fracture number can significantly reduce pressure depletion for small fracture conductivity ($C_{fD} = 0.01$) under fractal case, which is consistent with the finding of Cipolla (2009) that "if a high-relative-conductivity primary fracture can be created, the effect of primary fracture spacing is small".

To reveal further the effect of fracture number on flow regime evolution in the fractal case, the pressure derivatives in log–log coordinate are presented in Fig. 8c. It is found that fracture number is the main factor determining the finishing time of SRV-XRV bilinear flow, denoted by red triangle. With fracture number increasing, the effect of fracture interaction becomes stronger. Hence, pressure derivative will follow the XRV linear flow regime in advance, characterized by a 0.5-slope straight. At the same time, the duration of SRV-XRV bilinear flow would shorten, which changes from $t_D \approx 3 \sim 1000$ for $n_f = 2$ to $t_D \approx 3 \sim 70$ for $n_f = 5$. In addition, the pressure derivatives of late-time flow regime for different HF numbers are parallel distributed, not overlapping like homogeneity case. It illustrates that the effec-

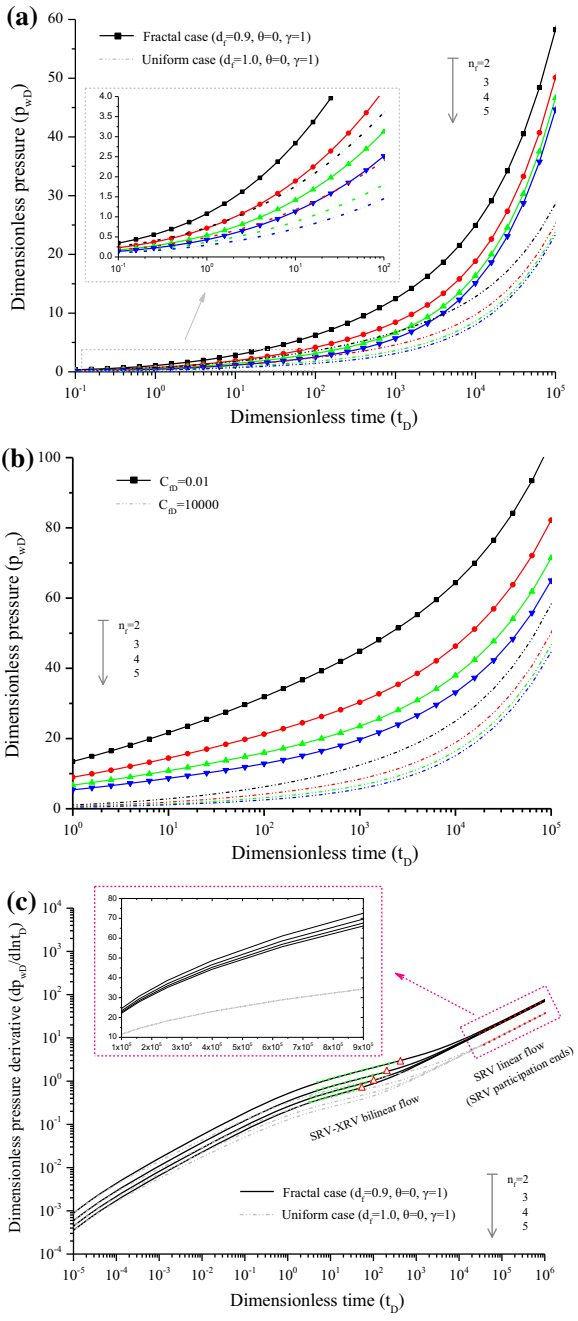

Fig. 8 **a** Effect of fracture number on pressure in fractal and uniform cases ($C_{fD} = 10^4$). **b** Effect of fracture number on pressure in large/small fracture conductivity ($d_f = 0.9, \theta = 0, \gamma = 1$). **c** Effect of fracture number on flow regime evolution in fractal and uniform cases ($C_{fD} = 10^4$)

tiveness of fracturing treatment would make difference during the whole production period of MFHW, which could be improved by creating strong-interconnected SRV (i.e., fractal dimension constant d_f gradually approximates to Euclidian dimension constant of 1).

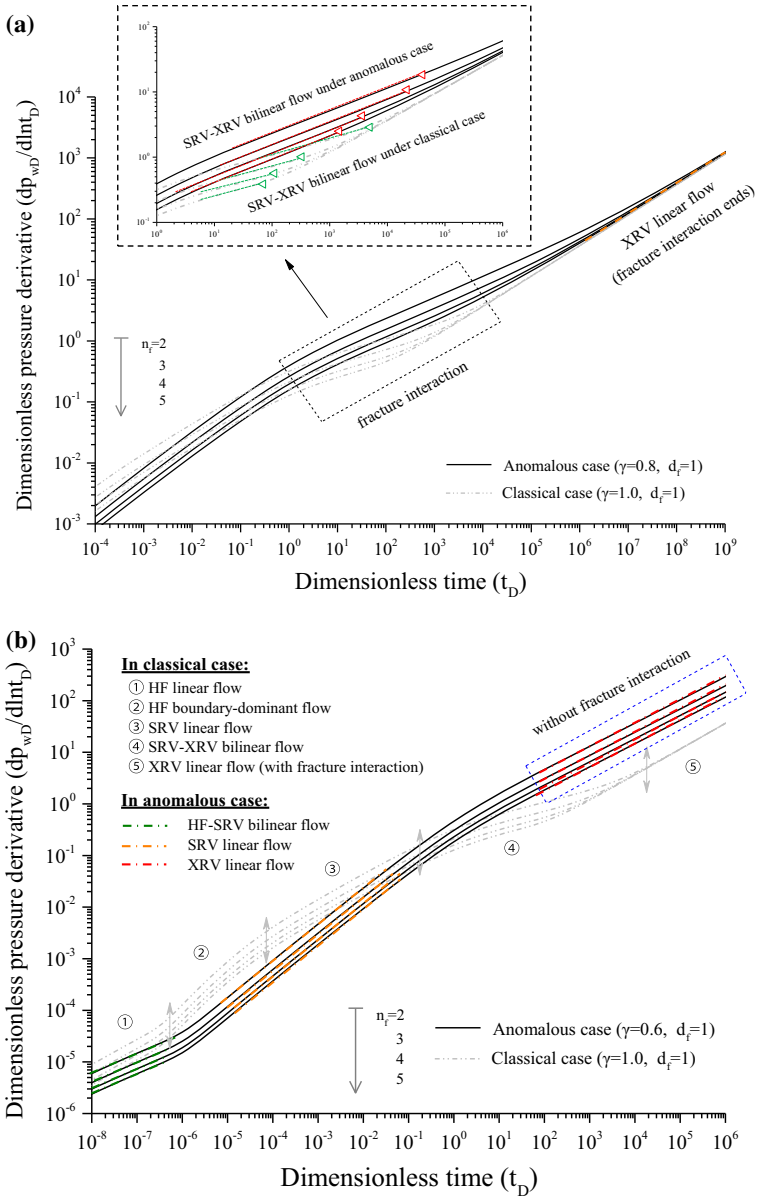

Fig. 9 Effect of fracture number on flow regime evolution in anomalous and classical cases ($C_{fD} = 10^4$)

5.2.2 Anomalous Diffusion Case

Figure 9 shows the effect of fracture number in the anomalous diffusion case ($\gamma < 1$). In this sub-illustration, the dimensionless fracture conductivity is set to be 10000. As seen in Fig. 9a, the type, sequence and duration of flow regime are identical with Sect. 5.1.2 before fracture–production interacts. As observed in the time interval of $t_D > 1$, anomalous diffusion will delay the occurring of fracture interaction, denoted by red triangular; taking

$n_f = 5$ for example, the occurring time of fracture interaction is about $t_D \approx 100$ for classical diffusion/homogeneity case, but changes to $t_D \approx 600$ for anomalous diffusion ($\gamma = 0.8$). Meanwhile, the duration of transition flow from SRV-XRV bilinear to XRV linear would elongate. We find that the HF interaction is not evident as anomalous diffusion constant decreases.

Figure 9b further shows the effect of anomalous diffusion. When γ decreases to a smaller enough value (i.e., $\gamma < 0.6$), the fracture interaction is absent completely, which indicates the anomalous diffusion makes fracture interaction weaker. Moreover, in the case of strong anomalous diffusion ($\gamma < 0.6$), the pressure curves during the XRV linear-regime period are distributed more sparsely. Therefore, increasing fracture number would reduce pressure depletion effectively, which is analogous to fractal case in Sect. 5.2.1.

6 Conclusions

In our work, a semi-analytical solution for multi-fractured horizontal well with fractal geometry is established, and an accurate algorithm is proposed to interpret the transient pressure behavior. Several principal contributions are further summarized below:

(1) In this paper, we focus on the heterogeneity of SRV and multiple-fractured configuration on transient pressure behavior. A general model accounting for the characteristics of fractured media has been proposed.
(2) The semi-analytical solution accounts for the effect of permeability alteration within SRV and arbitrary properties of HFV. The newly presented algorithm is complete, rigorous, computationally stable and accurate.
(3) Fractal geometry contributes to greater pressure depletion during the whole flow period, while anomalous diffusion contribute to smaller pressure depletion at the early-flow period but becomes larger at the late-flow period.
(4) In the fractured reservoir with fractal geometry and anomalous diffusion, the effect of HF conductivity on pressure behavior become weaker, but the effect of HF number is stronger.
(5) The characteristic of fractal geometry and anomalous diffusion makes fracture–production interaction weaker; the characteristic of intermediate-time flow regimes tend to be similar, which results in long linear-trending production period in field test.

Acknowledgments The authors are indebted to Professor Ailin Jia and Dongbo He in RIPED for their great support and Schlumberger Eclipse for use of their black oil simulator. Thanks are owed to the anonymous reviewers for their insightful and constructive comments for improving the manuscript. This article was supported by the National Major Research Program for Science and Technology of China (No. 211ZX05015).

Appendix 1: Anomalous Diffusion in Fractal Porous Media

Fractal Porous Media

In the porous media, the feature of fracture and fracture network is generally represented by two fundamental parameters: permeability and porosity. Chang and Yortsos (1990) were the first authors adopting a fractal model to describe fractured reservoirs. In Chang's fractal model, the permeability and porosity are firstly described as power-law relations, respectively:

$$\phi = \frac{aV_s}{G} \cdot r^{d_f - d_e} \tag{17}$$

$$k = \frac{aV_s m}{G} \cdot r^{d_f - d_e - \theta} \tag{18}$$

where d_f is mass fractal dimension (embedded in the Euclidean matrix), d_e is Euclidean dimension (always an integer, $d_e = 1$ for 1D case, $d_e = 2$ for 2D case), θ is conductivity index reflecting the anomaly in conductivity in fractal object ($\theta = 0$ indicates the classical random walk), a is site density parameter, m is fracture-network parameter, V_s is volume per site, G is geometry factor, k is permeability and φ is porosity. Here we should emphasis that Eqs. (17) and (18) do not correspond to point value but to the porosity and permeability of regions of size r, only suggesting all properties of any region of size r are scale-dependent following a power law in a fractal medium [seen in the dissertation of Cissio (2012) for integrated explanation].

Anomalous Diffusion

As consequence, non-local and memory effect in fractal-like structure needs to be considered to account for the associated anomalous diffusion in highly complex media with fractal geometry [seen Raghavan (2012a, b), Raghavan et al. (2013a, b) and Chen and Raghavan (2013, 2015) for the detailed explanation and analysis of fractional diffusion effect on production performance of MFHW]. This essentially differs from conventional Darcy formation used in the induced flow capacity model. Through using Continue Time Random Walk (CTRW) model presented by Raghavan (2012a), anomalous diffusion is presented by the modified Darcy rate in a convolved form:

$$\vec{v} = -\frac{k}{\mu}\frac{\partial}{\partial t}\int_0^t \frac{\nabla p}{(t-t')^{1-\gamma}} dt' \tag{19}$$

where the constant γ builds a relation between fractal structure model and anomalous diffusion, $\gamma = \frac{2}{2+\theta}$. Thus, $\theta = 0$ indicates the classical random walk/diffusion, namely described by traditional Darcy formula. More specifically, it is described as sub-diffusive if $\theta > 0$ and super-diffusive if $\theta < 0$. According to Caputo fractional operator (1967), modified Darcy law is presented in the form of fractional derivative,

$$\vec{v} = -\frac{k}{\mu}\frac{\partial^{1-\gamma}\nabla p}{\partial t^{1-\gamma}} \tag{20}$$

The anomalous diffusion provides new insight into the transport process throughout fractal-like porous media and improves PTA and RTA interpretations [e.g., linear trend of production rate over exceedingly long time in fractured reservoirs presented by Raghavan et al. (2013a); the faster or slower rate decline from complex reservoirs than classical diffusion in early-time response presented by Chen and Raghavan (2013)].

Appendix 2: Dimensionless Definitions

The dimensionless pressure, time respectively are given as,

$$p_{\xi D} = \frac{2\pi k_{\text{ref}} h}{q_{\text{ref}} \mu c_t}(p_i - p_\zeta), \quad \zeta = \text{HF, SRV, XRV} \tag{21}$$

$$t_{\mathrm{D}} = \frac{k_{\mathrm{ref}}}{\phi_{\mathrm{ref}} c L_{\mathrm{ref}}^2} t \tag{22}$$

In the hydraulic fracture model, the dimensionless fracture conductivity, C_{HFD}, is

$$C_{\mathrm{HFD}} = \frac{k_{\mathrm{HF}} w_{\mathrm{HF}}}{k_{\mathrm{ref}} L_{\mathrm{ref}}} \tag{23}$$

Note that the dimensionless fracture conductivity is defined with the reference length and reference permeability.

The dimensionless hydraulic fracture diffusivity is given as

$$\eta_{\mathrm{HFD}} = \frac{k_{\mathrm{HF}} \phi_{\mathrm{ref}}}{\phi_{\mathrm{HF}} k_{\mathrm{ref}}} \tag{24}$$

The dimensionless diffusivity of SRV is given as

$$\eta_{\mathrm{SRVD}} = \frac{k_{\mathrm{SRV}}^{\mathrm{ref}}}{k_{\mathrm{ref}}} \left(\frac{\phi_{\mathrm{ref}} \mu c L_{\mathrm{ref}}^2}{k_{\mathrm{ref}}} \right)^{\gamma - 1} \tag{25}$$

The dimensionless diffusivity of XRV is given as

$$\eta_{\mathrm{XRVD}} = \frac{k_{\mathrm{XRV}} / \phi_{\mathrm{XRV}}}{k_{ref} / \phi_{\mathrm{ref}}} \tag{26}$$

The flow capacity ratio between SRV and HF is given,

$$\lambda_{\mathrm{HF}}^{\mathrm{SRV}} = \frac{k_{\mathrm{SRV}}^{\mathrm{ref}} L_{\mathrm{ref}}}{k_{\mathrm{HF}} w_{\mathrm{HF}}} \left(\frac{w_{\mathrm{HF}}}{2 L_{\mathrm{ref}}} \right)^{d_f - d_e - \theta} \left(\frac{\phi_{\mathrm{ref}} \mu c L_{\mathrm{ref}}^2}{k_{\mathrm{ref}}} \right)^{\gamma - 1} \tag{27}$$

The flow capacity ratio between XRV and SRV is given,

$$\lambda_{\mathrm{SRV}}^{\mathrm{XRV}} = \frac{k_{\mathrm{XRV}} L_{\mathrm{ref}} \phi_{\mathrm{ref}}}{k_{\mathrm{SRV}}^{\mathrm{ref}} x_{\mathrm{HF}}} \left(\frac{k_{\mathrm{ref}}}{\phi_{\mathrm{ref}} \mu c L_{\mathrm{ref}}^2} \right)^{\gamma - 1} \tag{28}$$

The dimensionless production rate of hydraulic fracture is defined as,

$$q_{\mathrm{HFD}} = \frac{q_{\mathrm{HF}}}{q_{\mathrm{ref}}} \tag{29}$$

The dimensionless length in 1D coordinates is

$$\xi_{\mathrm{D}} = \frac{\xi}{L_{\mathrm{ref}}}, \ \xi = x, y, x_R, x_f, L_s, w_{\mathrm{HF}} \tag{30}$$

Appendix 3: Flow Model and Solution for XRV

The fundamental partial differential equation that governs fluid flow into XRV is given in the 1D coordinate system by,

$$-\frac{\partial}{\partial x}(\rho \vec{v}_{\mathrm{XRV}}) = \phi_{\mathrm{XRV}} \frac{\partial \rho}{\partial t} \tag{31}$$

In dimensionless terms defined in Appendix B, Eq. (31) can be rewritten in Laplace-transform domain

$$\frac{\partial^2 \tilde{p}_{\mathrm{XRVD}}}{\partial x_{\mathrm{D}}^2} = \frac{s}{\eta_{\mathrm{XRVD}}} \tilde{p}_{\mathrm{XRVD}} \tag{32}$$

According to no-flow condition on outer boundary of XRV ($x = x_{\mathrm{R}}$) and coupling condition on interface between XRV and SRV ($x = x_{\mathrm{HF}}$), similar to Eq. (20)–(21) in the work of Brown et al. (2009), we could obtain the dimensionless flux on the interface between SRV and XRV region, as follows:

$$\left(\frac{\partial \tilde{p}_{\mathrm{XRVD}}}{\partial x_{\mathrm{D}}}\right)\Big|_{x_{\mathrm{D}}=x_{\mathrm{HFD}}} = -\tilde{F}_{\mathrm{SRV}}^{\mathrm{XRV}} \left(\tilde{p}_{\mathrm{SRVD}}|_{x_{\mathrm{D}}=x_{\mathrm{HFD}}}\right) \tag{33}$$

where $\tilde{F}_{\mathrm{SRV}}^{\mathrm{XRV}}$ is defined as the characteristic function representing the dimensionless flux from XRV to SRV, which is given as

$$\tilde{F}_{\mathrm{SRV}}^{\mathrm{XRV}} = \sqrt{\frac{s}{\eta_{\mathrm{XRVD}}}} \tanh\left[\sqrt{\frac{s}{\eta_{\mathrm{XRVD}}}} (x_{RD} - x_{\mathrm{HFD}})\right] \tag{34}$$

Appendix 4: Flow Model and Solution for SRV

Two coordinate systems are, respectively, established with respect to fracture plane. Within the REV, the flow equation in *Right/Left* side region is given as,

$$\frac{\partial(\rho \vec{v}_{\mathrm{SRV}}^{\xi})}{\partial y} + \frac{\partial(\rho \phi_{\mathrm{SRV}}^{\xi})}{\partial t} = 0 \tag{35}$$

Using fractal-geometry equation presented by Eqs. (1)–(2) and modified Darcy equation presented by Eq. (20), we could obtain pressure governing equation as,

$$\begin{aligned} &\frac{\partial^{1-\gamma_\xi}}{\partial t^{1-\gamma_\xi}} \left[\frac{\partial k_{\mathrm{SRV}}^{\xi}}{\partial y} \frac{\partial m_{\mathrm{SRV}}^{\xi}}{\partial y} + k_{\mathrm{SRV}}^{\xi} \frac{\partial^2 p_{\mathrm{SRV}}^{\xi}}{\partial y^2}\right] \\ &= -\phi_{\mathrm{SRV}} \left[\frac{k_{\mathrm{XRV}}}{x_{\mathrm{HF}}} \left(\frac{\partial p_{\mathrm{XRV}}}{\partial x}\right)\Big|_{x=x_{\mathrm{HF}}} - \mu c_t \frac{\partial p_{\mathrm{SRV}}^{\xi}}{\partial t}\right] \end{aligned} \tag{36}$$

The dimensionless pressure governing equation in Laplace-transform domain is rewritten as follows:

$$\frac{\partial^2 \tilde{p}_{\mathrm{SRVD}}^{\xi}}{\partial y_{\mathrm{D}}^2} + \frac{d_{f,\xi} - d_e - \theta_\xi}{y_{\mathrm{D}}} \frac{\partial \tilde{p}_{\mathrm{SRVD}}^{\xi}}{\partial y_{\mathrm{D}}} = y_{\mathrm{D}}^{\theta_\xi} \left(\frac{s^{\gamma_\xi}}{\eta_{\mathrm{SRVD}}^{\xi}} + \frac{\lambda_{\mathrm{SRV},\xi}^{\mathrm{XRV}} \tilde{F}_{\mathrm{SRV},\xi}^{\mathrm{XRV}}}{s^{1-\gamma_\xi}}\right) \tilde{p}_{\mathrm{SRVD}}^{\xi} \tag{37}$$

where, ξ represents the *Right/Left* side region or *Middle* point between right- and left-side region within REV.

Solution for Outermost REV

The dimensionless pressure is continuous in the interface between SRV and HFV, $\tilde{p}^{\xi}_{\mathrm{SRVD}}(0.5w_{\mathrm{HFD}}) = \tilde{p}^{\xi}_{\mathrm{HFD}}$, and the condition is no-flow on the outermost boundary of SRV,

$$\left(\frac{\partial \tilde{p}^{\xi}_{\mathrm{SRVD}}}{\partial y_{\mathrm{D}}}\right)\Bigg|_{y_{\mathrm{D}}=L_{mD,\xi}} = 0. \tag{38}$$

Equation (33) is a general form of the modified Bessel differential equation. According to the general solution presented by Bowman (1958), the dimensionless flux on interface between SRV and HF could be obtained,

$$\left(\frac{\partial \tilde{p}^{\xi}_{\mathrm{SRVD}}}{\partial y_{\mathrm{D}}}\right)\Bigg|_{y_{\mathrm{D}}=0.5w_{\mathrm{HFD}}} = -\tilde{F}^{\mathrm{SRV}}_{\mathrm{HF},\xi}\left(\tilde{p}^{\xi}_{\mathrm{HFD}}\Big|_{y_{\mathrm{D}}=0.5w_{\mathrm{HFD}}}\right) \tag{39}$$

where $\tilde{F}^{\mathrm{SRV}}_{\mathrm{HF}}$ indicates the influx supply from SRV into HF.

$$\tilde{F}^{\mathrm{SRV}}_{\mathrm{HF},\xi} = \frac{b_\xi c_\xi w^{c_\xi-1}_{\mathrm{HFD}}}{2^{c_\xi-1}} \frac{I_{n_\xi-1}(b_\xi L^{c_\xi}_{mD})K_{n_\xi-1}(0.5^{c_\xi} b_\xi w^{c_\xi}_{\mathrm{HFD}}) - K_{n_\xi-1}(b_\xi L^{c_\xi}_{mD})I_{n-1}(0.5^{c_\xi} b_\xi w^{c_\xi}_{\mathrm{HFD}})}{I_{n_\xi}(0.5^{c_\xi} b_\xi w^{c_\xi}_{\mathrm{HFD}})K_{n_\xi-1}(0.5^{c_\xi} b_\xi L^{c_\xi}_{sD}) + K_{n_\xi}(0.5^{c_\xi} b_\xi w^{c_\xi}_{vHFD})I_{n-1}(b_\xi L^{c_\xi}_{mD})} \tag{40}$$

Solution for Inner REV

Boundary Condition 1: The dimensionless pressure is continuous in the interface between SRV and HFV, which is respectively satisfied as,

For left-side region:

$$\tilde{p}^{\mathrm{L}}_{\mathrm{SRVD}}(0.5w_{\mathrm{HFD}}) = \tilde{p}^{\mathrm{L}}_{\mathrm{HFD}};\ \ \tilde{p}^{\mathrm{L}}_{\mathrm{SRVD}}(L_{mD}) = \tilde{p}^{M}_{\mathrm{HFD}} \tag{41}$$

For right-side region:

$$\tilde{p}^{\mathrm{R}}_{\mathrm{SRVD}}(0.5w_{\mathrm{HFD}}) = \tilde{p}^{\mathrm{R}}_{\mathrm{HFD}};\ \ \tilde{p}^{\mathrm{R}}_{\mathrm{SRVD}}(L_{sD} - L_{mD}) = \tilde{p}^{M}_{\mathrm{HFD}} \tag{42}$$

Boundary Condition 2: the flux continuity on the interface between *Right* and *Left* SRV region is given as

$$\left(\frac{\partial \tilde{p}^{\mathrm{L}}_{\mathrm{SRVD}}}{\partial y_{\mathrm{D}}}\right)\Bigg|_{y_{\mathrm{D}}=L_{mD}} + \left(\frac{\partial \tilde{p}^{\mathrm{R}}_{\mathrm{SRVD}}}{\partial y_{\mathrm{D}}}\right)\Bigg|_{y_{\mathrm{D}}=L_{sD}-L_{mD}} = 0 \tag{43}$$

Anomalous to the derivation in Section D1, the dimensionless influx on the surface of HF, as follows:

$$\left(\frac{\partial \tilde{p}^{\mathrm{L}}_{\mathrm{SRVD}}}{\partial y_{\mathrm{D}}}\right)\Bigg|_{y_{\mathrm{D}}=0.5w_{\mathrm{HFD}}} = \tilde{F}^{\mathrm{SRV}}_{HF,R1}\left(\tilde{p}^{\mathrm{R}}_{\mathrm{HFD}}\big|_{y_{\mathrm{D}}=0.5w_{\mathrm{HFD}}}\right) - \tilde{F}^{\mathrm{SRV}}_{HF,L1}\left(\tilde{p}^{\mathrm{L}}_{\mathrm{HFD}}\big|_{y_{\mathrm{D}}=0.5w_{\mathrm{HFD}}}\right) \tag{44}$$

$$\left(\frac{\partial \tilde{p}^{\mathrm{R}}_{\mathrm{SRVD}}}{\partial y_{\mathrm{D}}}\right)\Bigg|_{y_{\mathrm{D}}=w_{\mathrm{HFD}}/2} = \tilde{F}^{\mathrm{SRV}}_{HF,R2}\left(\tilde{p}^{\mathrm{R}}_{\mathrm{HFD}}\big|_{y_{\mathrm{D}}=0.5w_{\mathrm{HFD}}}\right) - \tilde{F}^{\mathrm{SRV}}_{HF,L2}\left(\tilde{p}^{\mathrm{L}}_{\mathrm{HFD}}\big|_{y_{\mathrm{D}}=0.5w_{\mathrm{HFD}}}\right) \tag{45}$$

where

$$\tilde{F}^{\mathrm{SRV}}_{HF,R1} = -\left(\frac{w_{\mathrm{HFD}}}{2}\right)^{a_L+c_L-1-a_R}\frac{(L_{sD}-L_{mD})^{a_R+c_R-1}\Psi_{R1}}{L_{mD}^{a_L}\Theta} \tag{46}$$

$$\tilde{F}^{\mathrm{SRV}}_{\mathrm{HF},L2} = -\left(\frac{w_{\mathrm{HFD}}}{2}\right)^{a_R+c_R-1-a_L}\frac{L_{mD}^{a_L+c_L-1}\Psi_{L2}}{(L_{sD}-L_{mD})^{a_R}\Theta} \tag{47}$$

$$\tilde{F}^{\mathrm{SRV}}_{\mathrm{HF},L1} = -\left(\frac{w_{\mathrm{HFD}}}{2}\right)^{c_L-1}\left(\frac{E_{L1}\Theta+L_{mD}^{c_L-1}\Psi_{L1}}{\Theta}\right) \tag{48}$$

$$\tilde{F}^{\mathrm{SRV}}_{HF,R2} = -\left(\frac{w_{\mathrm{HFD}}}{2}\right)^{c_R-1}\left(\frac{E_{R2}\Theta+(L_{sD}-L_{mD})^{c_R-1}\Psi_{R2}}{\Theta}\right) \tag{49}$$

Relative relationships used are list as follows:

$$\Theta = \sum_{i=1}^{2} b_\xi c_\xi L_{\mathrm{D},\xi}^{c_\xi-1}\frac{K_{n_\xi}(\delta_{\xi,1})I_{n_\xi-1}(\delta_{\xi,2})+K_{n_\xi-1}(\delta_{\xi,2})I_{n_\xi}(\delta_{\xi,1})}{K_{n_\xi}(\delta_{\xi,2})I_{n_\xi}(\delta_{\xi,1})-K_{n_\xi}(\delta_{\xi,1})I_{n_\xi}(\delta_{\xi,2})} \tag{50}$$

$$\Psi_{R1} = \prod_{i=1}^{2} b_\xi c_\xi \frac{K_{n_\xi}(\delta_{\xi,i})I_{n_\xi-1}(\delta_{\xi,i})+K_{n_\xi-1}(\delta_{\xi,i})I_{n_\xi}(\delta_{\xi,i})}{K_{n_\xi}(\delta_{\xi,2})I_{n_\xi}(\delta_{\xi,1})-K_{n_\xi}(\delta_{\xi,1})I_{n_\xi}(\delta_{\xi,2})} \tag{51}$$

$$\Psi_{L2} = \prod_{i=1}^{2} b_\xi c_\xi \frac{K_{n_\xi}(\delta_{\xi,k})I_{n_\xi-1}(\delta_{\xi,k})+K_{n_\xi-1}(\delta_{\xi,k})I_{n_\xi}(\delta_{\xi,k})}{K_{n_\xi}(\delta_{\xi,2})I_{n_\xi}(\delta_{\xi,1})-K_{n_\xi}(\delta_{\xi,1})I_{n_\xi}(\delta_{\xi,2})}, \quad k=\begin{cases}2, & \text{if i}=1\\ 1, & \text{if i}=2\end{cases} \tag{52}$$

$$\Psi_{L1} = \prod_{i=1}^{2} b_L c_L \frac{K_{n_L}(\delta_{L,i})I_{n_L-1}(\delta_{L,i})+K_{n_L-1}(\delta_{L,i})I_{n_L}(\delta_{L,i})}{K_{n_L}(\delta_{L,2})I_{n_L}(\delta_{L,1})-K_{n_L}(\delta_{L,1})I_{n_L}(\delta_{L,2})} \tag{53}$$

$$\Psi_{R2} = \prod_{i=1}^{2} b_R c_R \frac{K_{n_R}(\delta_{R,i})I_{n_R-1}(\delta_{R,i})+K_{n_R-1}(\delta_{R,i})I_{n_R}(\delta_{R,i})}{K_{n_R}(\delta_{R,2})I_{n_R}(\delta_{R,1})-K_{n_R}(\delta_{R,1})I_{n_R}(\delta_{R,2})} \tag{54}$$

when $i=1,\xi$ denotes *Left* and $L_{\mathrm{D},\xi}=L_{\mathrm{mD}}$; when $i=2,\xi$ denotes *Right* and $L_{\mathrm{D},\xi}=L_{\mathrm{sD}}-L_{\mathrm{mD}}$. Meanwhile,

$$E_{L1} = b_L c_L \frac{K_{n_L}(\delta_{L,2})I_{n_L-1}(\delta_{L,1})+K_{n_L-1}(\delta_{L,1})I_{n_L}(\delta_{L,2})}{K_{n_L}(\delta_{L,2})I_{n_L}(\delta_{L,1})-K_{n_L}(\delta_{L,1})I_{n_L}(\delta_{L,2})} \tag{55}$$

$$E_{R2} = b_R c_R \frac{K_{n_R}(\delta_{R,2})I_{n_R-1}(\delta_{R,1})+K_{n_R-1}(\delta_{R,1})I_{n_R}(\delta_{R,2})}{K_{n_R}(\delta_{R,2})I_{n_R}(\delta_{R,1})-K_{n_R}(\delta_{R,1})I_{n_R}(\delta_{R,2})} \tag{56}$$

And

$$\delta_{\xi,1} = 0.5 b_\xi c_\xi w_{HFD}, \quad \delta_{\xi,2} = b_\xi c_\xi L_{\mathrm{D},\xi} \tag{57}$$

$$a_\xi = \frac{\theta_\xi + d_e - d^+_{f,\xi} 1}{2} \tag{58}$$

$$b_\xi = \left(\frac{2}{\theta_\xi} + 2\right) \sqrt{s^{\gamma_\xi - 1}\left(\frac{s}{\eta^\xi_{SRVD}} + \lambda^{\mathrm{XRV}}_{\mathrm{SRV},\xi} \tilde{F}^{\mathrm{XRV}}_{\mathrm{SRV},\xi}\right)} \tag{59}$$

$$c_\xi = \frac{\theta_\xi + 2}{2} \tag{60}$$

$$n_\xi = \frac{a_\xi}{c_\xi} \tag{61}$$

Appendix 5: Flow Model and Solution for HFV

In single REV, the flow equations in the right or left half-HF are given by,

$$\frac{\partial(\rho \vec{v}^\xi_{HF})}{\partial x} + \frac{2}{w_{\mathrm{HF}}}\left(\rho \vec{v}^\xi_{\mathrm{SRV}}\right)\Big|_{y=w_{\mathrm{HF}}/2} + \frac{\partial(\rho \phi^\xi_{\mathrm{HF}})}{\partial t} = 0 \tag{62}$$

Incorporating fractal-geometry equation presented by Eqs. (1)–(2) and modified Darcy equation presented by Eq. (20), we use dimensionless definition as Appendix B to deal with Eq. (62). Hence, the dimensionless pressure is given in Laplace-transform domain as,

$$\frac{\partial^2 \tilde{p}^\xi_{\mathrm{HFD}}}{\partial x^2_{\mathrm{D}}} + 2\frac{\lambda^{\mathrm{SRV}}_{\mathrm{HF},\xi}}{s^{\gamma_\xi - 1}}\left(\frac{\partial \tilde{p}^\xi_{\mathrm{SRVD}}}{\partial y_{\mathrm{D}}}\right)\Big|_{y_{\mathrm{D}}=w_{\mathrm{HFD}}/2} = \frac{s\tilde{p}_{\mathrm{HFD}}}{\eta_{\mathrm{HFD}}} \tag{63}$$

Boundary Condition 1: The flux rate from the region beyond hydraulic fracture tip into HFV is neglected ($x_{\mathrm{D}} = x_{\mathrm{HFD}}$),

$$\left(\frac{\partial \tilde{p}^\xi_{\mathrm{HFD}}}{\partial x_{\mathrm{D}}}\right)\Big|_{x_{\mathrm{D}}=x_{\mathrm{HFD}}} = 0 \tag{64}$$

Boundary Condition 2: The flux rate along half-width fracture into horizontal wellbore is given by

$$\left(\frac{\partial \tilde{p}^\xi_{\mathrm{HFD}}}{\partial x_{\mathrm{D}}}\right)\Big|_{x_{\mathrm{D}}=0} = -\frac{2\pi}{C^\xi_{\mathrm{HFD}}}\tilde{q}^\xi_{\mathrm{HFD}} \tag{65}$$

where $\xi = Left$ or $Right$. Taking Fourier cosine transformation and inversion transformation, we can obtain the solution for Eq. (63).

Solution for Outermost REV

For outermost REV,

$$\tilde{p}^{\xi}_{\mathrm{HFD}}(x_{\mathrm{D}}) = \frac{2\pi\tilde{q}^{\xi}_{HFD}}{C^{\xi}_{\mathrm{HFD}}}\left(\frac{s}{\eta^{\xi}_{HFD}} + \frac{2\lambda^{\mathrm{SRV}}_{\mathrm{HF},\xi}\tilde{F}^{\mathrm{SRV}}_{\mathrm{HF},\xi}}{s^{\gamma_\xi}-1}\right)^{-1/2} \coth\left(x_{\mathrm{HFD}}\sqrt{\frac{s}{\eta^{\xi}_{\mathrm{HFD}}} + \frac{2\lambda^{\mathrm{SRV}}_{HF,\xi}\tilde{F}^{\mathrm{SRV}}_{HF,\xi}}{s^{\gamma_\xi}-1}}\right) \tag{66}$$

$\tilde{F}^{\mathrm{SRV}}_{\mathrm{HF}}$ is the characteristic function which has been defined in Appendix D1.

Solution for Inner REV

For inner REV

$$\tilde{p}^{\mathrm{L}}_{\mathrm{HFD}}(x_{\mathrm{D}}) = AX^{\mathrm{L}}_{\mathrm{SRV}}(x_{\mathrm{D}})\tilde{q}^{\mathrm{L}}_{\mathrm{HFD}} + BX^{\mathrm{L}}_{\mathrm{SRV}}(x_{\mathrm{D}})\tilde{q}^{\mathrm{R}}_{\mathrm{HFD}} \tag{67}$$

$$\tilde{p}^{\mathrm{R}}_{\mathrm{HFD}}(x_{\mathrm{D}}) = AX^{\mathrm{R}}_{\mathrm{SRV}}(x_{\mathrm{D}})\tilde{q}^{\mathrm{R}}_{\mathrm{HFD}} + BX^{\mathrm{R}}_{\mathrm{SRV}}(x_{\mathrm{D}})\tilde{q}^{\mathrm{L}}_{\mathrm{HFD}} \tag{68}$$

where

$$AX^{\mathrm{L}}_{\mathrm{SRV}} = 2\pi\sum_{m=0}^{\infty}\frac{\cos(\beta_m x_{\mathrm{D}})}{N_m C^{\mathrm{L}}_{\mathrm{HFD}}\Lambda_L}\left(\beta_m^2 + 2\frac{\lambda^{\mathrm{SRV}}_{\mathrm{HF},R}\tilde{F}^{\mathrm{SRV}}_{HF,R2}}{s^{\gamma_L}-1} + \frac{s}{\eta^{\mathrm{R}}_{HFD}}\right) \tag{69}$$

$$BX^{\mathrm{L}}_{\mathrm{SRV}} = 4\pi\sum_{m=0}^{\infty}\frac{\cos(\beta_m x_{\mathrm{D}})}{N_m C^{\mathrm{L}}_{\mathrm{HFD}}\Lambda_L}\frac{\lambda^{\mathrm{SRV}}_{\mathrm{HF},L}\tilde{F}^{SRV}_{\mathrm{HF},R1}}{s^{\gamma_L}-1} \tag{70}$$

$$AX^{\mathrm{R}}_{\mathrm{SRV}} = 2\pi\sum_{m=0}^{\infty}\frac{\cos(\beta_m x_{\mathrm{D}})}{N_m C^{\mathrm{R}}_{\mathrm{HFD}}\Lambda_R}\left(\beta_m^2 + 2\frac{\lambda^{\mathrm{SRV}}_{HF,L}\tilde{F}^{\mathrm{SRV}}_{HF,L1}}{s^{\gamma_R}-1} + \frac{s}{\eta^{\mathrm{L}}_{\mathrm{HFD}}}\right) \tag{71}$$

$$BX^{\mathrm{R}}_{\mathrm{SRV}} = 4\pi\sum_{m=0}^{\infty}\frac{\cos(\beta_m x_{\mathrm{D}})}{N_m C^{\mathrm{R}}_{\mathrm{HFD}}\Lambda_R}\frac{\lambda^{\mathrm{SRV}}_{HF,R}\tilde{F}^{\mathrm{SRV}}_{HF,L2}}{s^{\gamma_R}-1} \tag{72}$$

and

$$\Lambda_L = \left(\beta_m^2 + 2\frac{\lambda^{SRV}_{\mathrm{HF},L}\tilde{F}^{\mathrm{SRV}}_{\mathrm{HF},L1}}{s^{\gamma_L}-1} + \frac{s}{\eta^{\mathrm{L}}_{HFD}}\right)\left(\beta_m^2 + 2\frac{\lambda^{\mathrm{SRV}}_{\mathrm{HF},R}\tilde{F}^{\mathrm{SRV}}_{HF,R2}}{s^{\gamma_L}-1} + \frac{s}{\eta^{\mathrm{R}}_{HFD}}\right) - 4\frac{\lambda^{SRV}_{\mathrm{HF},L}\lambda^{\mathrm{SRV}}_{\mathrm{HF},R}\tilde{F}^{\mathrm{SRV}}_{\mathrm{HF},R1}\tilde{F}^{\mathrm{SRV}}_{\mathrm{HF},L2}}{s^{2\gamma_L}-2} \tag{73}$$

$$\Lambda_R = \left(\beta_m^2 + 2\frac{\lambda^{\mathrm{SRV}}_{\mathrm{HF},L}\tilde{F}^{\mathrm{SRV}}_{\mathrm{HF},L1}}{s^{\gamma_R}-1} + \frac{s}{\eta^{\mathrm{L}}_{\mathrm{HFD}}}\right)\left(\beta_m^2 + 2\frac{\lambda^{\mathrm{SRV}}_{\mathrm{HF},R}\tilde{F}^{\mathrm{SRV}}_{\mathrm{HF},R2}}{s^{\gamma_R}-1} + \frac{s}{\eta^{\mathrm{R}}_{\mathrm{HFD}}}\right) - 4\frac{\lambda^{\mathrm{SRV}}_{\mathrm{HF},L}\lambda^{\mathrm{SRV}}_{\mathrm{HF},R}\tilde{F}^{\mathrm{SRV}}_{\mathrm{HF},R1}\tilde{F}^{\mathrm{SRV}}_{\mathrm{HF},L2}}{s^{2\gamma_R}-2} \tag{74}$$

$$\beta_m = \frac{m\pi}{x_{\mathrm{HFD}}}, m = 0, 1, 2, 3\cdots; N_m = \int_0^{x_{\mathrm{HFD}}}\cos^2(\beta_m x_{\mathrm{D}})\mathrm{d}x_{\mathrm{D}} = \begin{cases} 0.5x_{\mathrm{HFD}}, & m > 0 \\ x_{vHFD}, & m = 0 \end{cases} \tag{75}$$

References

Adler, P.M., Thovert, J.F.: Fractures and Fracture Networks Theory and Applications of Transport in Porous Media. Springer, Dordrecht (1999)

Bello, R.O., Wattenbarger, R.A.: Modeling and analysis of shale gas production with a skin effect. J. Can. Pet. Technol. **49**(12), 37–48 (2010)

Bowman, F.: Introduction to Bessel Functions. Dover Publications Edition, New York (1958)

Brown, M., Ozkan, E., Raghavan, R., et al.: Practical solutions for pressure-transient responses of fractured horizontal wells in unconventional shale reservoirs. Paper SPE 125043 presented at the SPE Annual Technical Conference and Exhibition, New Orleans, USA, 4–7 Octorber (2009)

Cai, J.C., Yu, B.M.: A discussion of the effect of tortuosity on the capillary imbibition in porous media. Transp. Porous Media **89**, 251–263 (2011)

Cai, J.C., Luo, L., Ye, R., et al.: Recent advances on fractal modeling of permeability for fibrous media. Fractals **23**(1), 1540006 (2015)

Camacho-Velázquez, R., Fuentes-Cruz, G., Vásquez-Cruz, M.: Decline-curve analysis of fractured reservoirs with fractal geometry. SPE Reserv. Eval. Eng. **6**, 606–619 (2008)

Caputo, M.: Linear models of dissipation whose Q is almost frequency independent-II. Geophys. J. Int. **13**(5), 529–539 (1967)

Chang, J.C., Yortsos, Y.C.: Pressure-transient analysis of fractal reservoirs. SPE Form. Eval. **3**, 31–38 (1990)

Chen, C., Raghavan, R.: Transient flow in a linear reservoir for space-time fractional diffusion. J. Pet. Sci. Eng. **128**, 194–202 (2015)

Chen, C., Raghavan, R.: On the liquid-flow analog to evaluate gas wells producing in shales. SPE Reserv. Eval. Eng. **5**, 209–215 (2013)

Chen, C.C., Raghavan, R.: A multiply-fractured horizontal well in rectangular drainage region. SPE J. **2**(11), 455–465 (1997)

Cipolla, C.L.: Modeling production and evaluating fracture performance in unconventional gas reservoirs. J. Pet. Technol. **9**, 84–90 (2009)

Cipolla, C.L., Fitzpatrick, T., Williams, M.J. et al.: Seismic-to-simulation for unconventional reservoir development. Paper SPE 146876 presented at the SPE Reservoir Characterisation and Simulation Conference and Exhibition, Abu Dhabi, UAR, 9–11 Octorber (2011)

Clarkson, C.R.: Production data analysis of unconventional gas wells: review of theory and best practices. Int. J. Coal Geol. **109**, 101–146 (2013)

Cossio, M., Moridis, G.J., Blasingame, T.A.: A semianalytic solution for flow in finite-conductivity vertical fractures by use of fractal theory. SPE J. **2**, 83–96 (2013)

EI-Banbi, A.H., Wattenbarger, R.A.: Analysis of linear flow in gas well production. Paper SPE 39972 presented at the 1998 SPE Gas Technology Symposium, Calgary, Canda, 15–18 March (1998)

Fuentes-Cruz, G., Gildin, E., Valkó, P.P.: Analyzing production data from hydraulically fractured wells: the concept of induced permeability field. SPE Reserv. Eval. Eng. **5**, 220–232 (2014a)

Fuentes-Cruz, G., Gildin, E., Valkó, P.P.: On the analysis of production data: practical approaches for hydraulically fractured wells in unconventional reservoirs. J. Pet. Sci. Eng. **119**, 54–68 (2014b)

Fuentes-Cruz, G., Valkó, P.P.: Revisiting the dual-porosity/dual permeability modeling of unconventional reservoirs: the induced-interporosity flow field. SPE J. **2**, 125–141 (2015)

Mayerhofer, M.J., Lolon, E.P., Warpinski, N.R., et al.: What is stimulated reservoir volume. SPE Prod. Oper. **2**, 89–98 (2011)

Monifar, A.M., Varavei, A., Johns, R.T., et al.: Development of a coupled dual continuum and discrete fracture model for the simulation of unconventional reservoirs. Paper SPE 163647 presented at the SPE Reservoir Simulation Symposium, Woodlands, USA, 18–20 Februry (2013)

Obinna, E.D., Hassan, D.: A model for simultaneous matrix depletion into natural and hydraulic fracture networks. J. Nat. Gas Sci. Eng. **16**, 57–69 (2014)

Ozcan, O., Ozkan, E., Raghavan, R.: A trilinear flow model for a fractured horizontal well in a fractal unconventional reservoir. In: SPE170971, presented at the SPE Annual Technical Conference and Exhibition, Amsterdam, Netherlands, October 27–29 (2014)

Raghavan, R.: Fractional derivatives: application to transient flow. J. Pet. Sci. Eng. **80**, 7–13 (2012a)

Raghavan, R.: Fractional derivatives: performance of fractured well. J. Pet. Sci. Eng. **92–93**, 167–173 (2012b)

Raghavan, R., Chen, C.: Fractional diffusion in rocks produced by horizontal wells with multiple, transverse fractures of finite conductivity. J. Pet. Sci. Eng. **109**, 133–143 (2013a)

Raghavan, R., Chen, C.: Fractured-well performance under anomalous diffusion. SPE Reserv. Eval. Eng. **8**, 237–245 (2013b)

Song, B., Economides, M.J., Ehlig-Economides, C.: Design of multiple transverse fracture horizontal wells in shale gas reservoirs. Paper SPE-140555 presented at the SPE Hydraulic Fracturing Technology Conference and Exhibition, Texas, USA, 24–26 January (2011)

Stalgorova, E., Mattar, L.: Practical analytical model to simulate production of horizontal wells with branch fractures. Paper SPE 162515 presented at the SPE Canadian Unconventional Resources Conference, Calgary, Canada, 30 Octorber–1 November (2012)

Stalgorova, E., Mattar, L.: Analytical model for unconventional multifractured composite systems. SPE Reserv. Eval. Eng. **8**, 246–256 (2013)

Stehfest, H.: Numerical inversion of Laplace transforms algorithm. Commun. ACM **13**(1), 47–49 (1970)

Tivayanonda, V., Apiwathanasorn, S., Ehlig-Economides, C. et al.: Alternative interpretation of shale gas/oil rate behavior using a triple porosity model. Paper SPE 59703 presented at the SPE Annual Technical Conference and Exhibition, Texas, USA, 8–10 Octorber (2012)

Wang, J.L., Jia, A.L., Wei, Y.S.: A semi-analytical solution for multiple trilinear-flow model with asymmetry configuration in multifractured horizontal well. J. Nat. Gas Sci. Eng. (2016). doi:10.1016/j.jngse.2015.12.013

Wattenbarger, R.A., EI-Banbi, A.H., Villegas, M.E., et al.: Production analysis of linear flow into fractured tight gas wells. Paper SPE 39931 presented the 1998 Rocky Mountain Regional Symposium and Exhibition, Denver, Colorado, 5–8 April (1998a)

Weng, X., Kresse, O., Cohen, C., et al.: Modeling of hydraulic-fracture-network propagation in a naturally fractured formation. SPE Prod. Oper. **26**(4), 368–380 (2011)

Wu, Y.S., Ehlig-Economides, C., Qin, G. et al.: A triple-continuum pressure-transient model for a naturally fractured vuggy reservoir. Paper SPE 110044 presented at the 2007 SPE Annual Technical Conference and Exhibition, Anaheim, USA, 11–14 November (2007)

Zhao, Y.L., Zhang, L.H., Luo, J.X., et al.: Performance of fractured horizontal well with stimulated reservoir volume in unconventional gas reservoir. J. Hydrol. **512**, 447–456 (2014)